GEOSPHERE

GEOSPHERE, v. 20, no. 2

https://doi.org/10.1130/GES02701.1

14 figures; 2 tables; 2 sets of supplemental files (one set hosted externally)

CORRESPONDENCE: sakodama@ucsc.edu

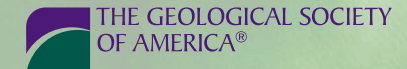
CITATION: Kodama, S.T., Cox, S.E., Thomson, S.N., Hemming, S.R., Williams, T., Licht, K.J., Formica, A., and Reiners, P.W., 2024, Multimethod dating of icerafted dropstones reveals hidden localized glacial erosion in Wilkes Subglacial Basin, Antarctica: Geosphere, v. 20, no. 2, p. 367–388, https://doi.org/10.1130/GES02701.1.

Science Editor: Andrea Hampel Associate Editor: James A. Spotila

Received 14 July 2023 Revision received 16 November 2023 Accepted 22 December 2023

Published online 8 March 2024





This paper is published under the terms of the CC-BY-NC license.

© 2024 The Authors

Multimethod dating of ice-rafted dropstones reveals hidden localized glacial erosion in Wilkes Subglacial Basin, Antarctica

Samuel T. Kodama¹, Stephen E. Cox², Stuart N. Thomson³, Sidney R. Hemming^{2,4}, Trevor Williams⁵, Kathy J. Licht⁶, Adam Formica⁴, and Peter W. Reiners³

Department of Earth and Planetary Sciences, University of California-Santa Cruz, Santa Cruz, California 95064, USA

²Lamont Doherty Earth Observatory, Columbia University, New York City, New York 10027, USA

³Department of Geosciences, University of Arizona, Tucson, Arizona 85721, USA

⁴Department of Earth and Environmental Sciences, Columbia University, New York City, New York 10027, USA

International Ocean Discovery Program, Texas A&M University, College Station, Texas 77845, USA

Department of Earth and Environmental Sciences, Indiana University Purdue University-Indianapolis, Indianapolis, Indiana 46202, USA

ABSTRACT

The Antarctic ice sheet blankets >99% of the continent and limits our ability to study how subglacial geology and topography have evolved through time. Ice-rafted dropstones derived from the Antarctic subglacial continental interior at different times during the late Cenozoic provide valuable thermal history proxies to understand this geologic history. We applied multiple thermochronometers covering a range of closure temperatures (60-800 °C) to 10 dropstones collected during Integrated Ocean Drilling Program (IODP) Expedition 318 in order to explore the subglacial geology and thermal and exhumation history of the Wilkes Subglacial Basin. The Wilkes Subglacial Basin is a key target for study because ice-sheet models show it was an area of ice-sheet retreat that significantly contributed to sea-level rise during past warm periods. Depositional ages of dropstones range from early Oligocene to late Pleistocene and have zircon U-Pb or 40Ar/39Ar ages indicating sources from the Mertz shear zone, Adélie craton, Ferrar large igneous province, and Millen schist belt. Dropstones from the Mertz shear zone and Adélie craton experienced three cooling periods (1700-1500 Ma; 500-280 Ma; 34-0 Ma) and two periods of extremely slow cooling rates (1500-500 Ma; 280-34 Ma). Low-temperature thermochronometers from seven of the dropstones record cooling during the Paleozoic, potentially recording the Ross or Pan-African orogenies, and during the Mesozoic, potentially recording late Paleozoic to Mesozoic rifting. These dropstones then resided within ~500 m of the surface since the late Paleozoic and early Mesozoic. In contrast, two dropstones deposited during the mid-Pliocene, one from the Mertz shear zone and one from Adélie craton, show evidence for localized post-Eocene glacial erosion of ≥2 km.

■ INTRODUCTION

With >99% of Antarctic bedrock hidden under ice (Burton-Johnson et al., 2016), offshore detrital geochronology and thermochronology of sediment derived from the subglacial Antarctic continental interior provide some of the only means of characterizing the bedrock geology of the continental interior (Pierce et al., 2014; Licht and Hemming,

Samuel T. Kodama https://orcid.org/0000-0002-1172-7366

2017), studying past ice-sheet dynamics (Williams et al., 2010; Zattin et al., 2012; Cook et al., 2013, 2017; Licht et al., 2014; Pierce et al., 2017), and investigating the exhumation history of subglacial topography (Cox et al., 2010; Tochilin et al., 2012; Thomson et al., 2013). Although offshore detrital mineral grain thermochronology is a powerful tool for understanding Antarctica's hidden bedrock, it can lack the detailed petrological, geochemical, and thermal-history context that a bedrock outcrop provides. Ice-rafted dropstones, clasts of bedrock

entrained by an ice sheet and then deposited offshore by melting icebergs, are a powerful archive, acting as mini-outcrops eroded by the ice sheet and deposited offshore. Each dropstone provides access to petrological information as well as multiple mineral chronometer systems that together can provide detailed information on provenance and thermal history of their hidden sources.

While multiple dating methods have been previously applied to clasts from Holocene terrestrial glacial deposits in Antarctica (e.g., Welke et al., 2016; Rolland et al., 2019; Voisine et al., 2020; Fitzgerald and Goodge, 2022), our study differs in applying multiple dating methods to ice-rafted dropstones of known and varying depositional ages, taken from marine core age models, including deposits older than the limits of cosmogenic nuclide exposure dating. Multimethod dating of dropstones that range in depositional age from the early Oligocene to the late Pleistocene enables us to obtain valuable insights into subglacial landscape evolution throughout the late Cenozoic. For example, areas that have undergone large-magnitude exhumation due to glacial erosion are likely inaccessible to terrestrial sampling methods because they are localized to ice streams (e.g., Naylor et al., 2021), which in Antarctica today are likely either covered by ice or ocean (submarine). However, bedrock eroded from these high-magnitude erosion areas can be accessed offshore due to iceberg transport. Therefore, multimethod dating of ice-rafted dropstones provides a key tool to understanding the topographic evolution of Antarctic subglacial topography.

Topography plays an important role in ice-sheet growth and stability in response to past climate change (Schoof, 2007; Austermann et al., 2015; Gasson et al., 2015; Colleoni et al., 2018; Pollard and DeConto, 2020; Paxman et al., 2020). Therefore, in order to best interpret ice-sheet records and test predictions of coupled ice sheet-climate models, we need to understand how the subglacial topography of Antarctica evolved through time. In areas like the Wilkes Subglacial Basin, where retrograde slopes (bed deepening inland) make the East Antarctic Ice Sheet unstable (Morlighem et al., 2020) and where previous provenance evidence has indicated dramatic fluctuations of the ice margin (Cook et al., 2013; Pierce et al., 2017; Wilson et al., 2018), understanding how the subglacial topography has changed is especially important. The subglacial topographic evolution of the Wilkes Subglacial Basin is not well constrained, with information restricted to estimates based on offshore sediment thickness and a combination of geomorphic analysis and flexural modeling (Paxman et al., 2018, 2019a) as well as a few coastal bedrock low-temperature thermochronology studies (Lisker and Olesch, 2003; Rolland et al., 2019; Voisine et al., 2020).

To further improve our understanding of the thermal history of Wilkes Subglacial Basin, and the post-Eocene evolution of the subglacial topography in the Wilkes Subglacial Basin, we present combinations of U-Pb zircon, U-Pb apatite, 40Ar/39Ar hornblende, 40Ar/39Ar biotite, 40Ar/39Ar muscovite, 40Ar/39Ar feldspar, (U-Th)/He zircon (ZHe), apatite fission-track (AFT), and (U-Th)/He apatite (AHe) ages (based on mineral availability) from 10 dropstones that were deposited offshore the Wilkes Subglacial Basin from the Oligocene to the late Pleistocene. We use these data to conduct HeFTy inverse thermal history modeling to produce time-temperature and time-depth histories to better understand the exhumation history and ice-sheet history of the Wilkes Subglacial Basin and compare estimates of exhumation to paleotopography reconstructions of the Wilkes Subglacial Basin (Paxman et al., 2019a) and previous coastal bedrock low-temperature thermochronology studies (Lisker and Olesch, 2003; Rolland et al., 2019; Voisine et al., 2020).

Summary of Wilkes Subglacial Basin Geology

Despite being mostly covered by ice, the geologic history of the Wilkes Subglacial Basin is relatively well constrained by sparse coastal outcrops, moraine deposits, and airborne geophysics (Peucat et al., 1999; Goodge et al., 2002, 2008, 2017; Ménot et al., 2007; Ferraccioli et al., 2009; Jordan et al., 2013; Aitken et al., 2014; Maritati et al., 2019; Naumenko-Dèzes et al., 2020; Swain and Kirby, 2021). The known geologic history allows us to trace the provenance of dropstones back to the continent. We can then use low-temperature thermochronometer ages paired with HeFTy inverse modeling to interpret the cooling, and therefore exhumational, history of the dropstone source.

The Wilkes Subglacial Basin is interpreted as a patchwork of four geochronologically defined domains: Terre Adélie, George V Land, Oates Land, and Northern Victoria Land (Ménot et al., 2007; Cook et al., 2013; Aitken et al., 2014; Naumenko-Dèzes et al., 2020). These terranes range in age from Neoarchean to Jurassic (Fig. 1). The oldest exposed bedrock in the Wilkes Subglacial Basin is Neoarchean granitoid rock found in Terre Adélie and George V Land that dates to 2600-2400 Ma (Peucat et al., 1999; Duclaux et al., 2008). These Neoarchean granitoids form part of the Adélie craton. The Adélie craton and overlying sedimentary basins were metamorphosed under upper-amphibolite-facies and granulite-facies conditions from 1700 to 1600 Ma (Peucat et al., 1999; Duclaux et al., 2008; Naumenko-Dèzes et al., 2020) and later underwent local shearing in the Mertz shear zone of George V Land ca. 1500 Ma (Di Vincenzo et al., 2007; Duclaux et al., 2008; Naumenko-Dèzes et al., 2020) and volcanism in the Gawler craton, forming the ca. 1595-1575 Ma Hiltaba Suite granites (Cooper et al., 1985; Chapman et al., 2019). Together, the Adélie and Gawler cratons formed the Mawson continent (Fig. 2; Payne et al., 2009).

The Wilkes Subglacial Basin does not have any exposed bedrock that shows direct tectonothermal influence from the Grenville orogeny (1300–1000 Ma); however, offshore detrital thermochronology and clasts from moraine deposits show evidence for both subglacial bedrock of Grenville orogeny age and bedrock with Grenville orogeny

overprinting (Goodge et al., 2010, 2017; Pierce et al., 2014).

Subduction processes at the margin of Gondwana, along what is now the eastern edge of the Wilkes Subglacial Basin, led to the Ross orogeny ca. 590–480 Ma (Federico et al., 2006; Di Vincenzo et al., 2007; Goodge, 2007). During the Ross orogeny in Northern Victoria Land, which borders Wilkes Subglacial Basin to the east, the Wilson, Bowers, and Robertson terranes and Millen schist belt formed through generally low-grade metamorphism and accretion of turbiditic rocks at this active continental margin (Estrada et al., 2016).

From the late Paleozoic into the Triassic, cooling and exhumation in the Lambert rift (Lisker et al., 2003), George V Land (Lisker and Olesch, 2003), and Bunger Hills (Maritati et al., 2020) are interpreted to represent intracontinental rifting (Maritati et al., 2020) that would have impacted Wilkes Subglacial Basin; however the oldest known faults in Terre Adélie are Proterozoic in age (Naumenko-Dèzes et al., 2020; Rolland et al., 2019). During the later initial Mesozoic breakup of Gondwana, rifting caused the emplacement of the Ferrar large igneous province in Northern Victoria Land and Oates Land ca. 180 Ma (Elliot, 1992; Fleming et al., 1997; Elliot and Fleming, 2004, 2018; Burgess et al., 2015). Finally, rifting throughout the mid- to late- Mesozoic and the early Cenozoic dispersed the Gondwanan continents and separated the Wilkes Subglacial Basin from southern Australia ca. 83 Ma (Boger, 2011; Veevers, 2012).

Summary of Cenozoic East Antarctic Ice Sheet History

An abrupt increase in δ^{18} O, changes in clay mineralogy, and introduction of ice-rafted detritus in sedimentologic records mark the initiation of continent-scale glaciation of Antarctica at the Eocene-Oligocene boundary (Zachos et al., 2001; Ehrmann and Mackensen, 1992; Diester-Haass et al., 1993; Robert and Kennett, 1997; Sagnotti et al., 1998). The Antarctic ice sheet advanced into the Wilkes Subglacial Basin during the early Oligocene, 33.5–30 Ma (Escutia et al., 2005) and fluctuated between 85% and 110% of the modern East Antarctic Ice

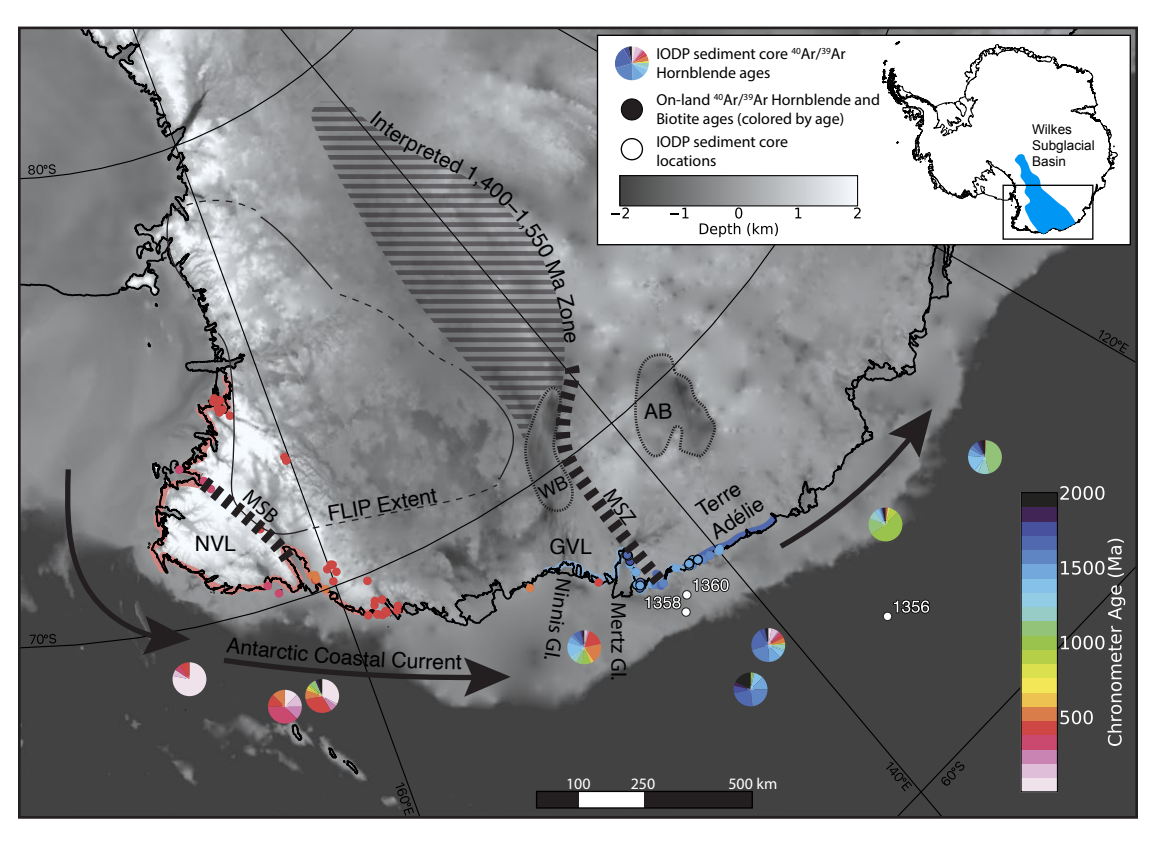


Figure 1. Topographic map of the Wilkes Subglacial Basin sector of East Antarctica (modified from Pierce et al., 2017; Morlighem et al., 2020). Pie charts show offshore core top age distributions of 40Ar/39Ar hornblende ages (Roy et al., 2007; Pierce et al., 2011, 2014). Black arrows show the direction of Antarctic Coastal Current that transports icebergs. Locations of Integrated Ocean **Drilling Program (IODP) Expedition** 318 drill sites 1356, 1358, and 1360 are labeled. Red and blue colored points show on-land 40Ar/39Ar hornblende and biotite ages (Duclaux et al., 2007, 2008; Di Vincenzo et al., 2007) with colors corresponding to ages as shown in the legend (Williams et al., 2010). Coastlines are highlighted with the corresponding predominant 40Ar/39Ar chronometer age. The extent of the Ferrar large igneous province (FLIP) is outlined (Ferraccioli et al., 2009). The Mertz shear zone (MSZ: shear zone activity from 1650 to 1600 Ma with reactivation until after 1500 Ma; Di Vincenzo et al., 2007; Naumenko-Dèzes et al., 2020) and Millen schist belt (MSB) are marked with thick dashed lines. Proposed inland extent of this 40Ar/39Ar 1550-1400 Ma zone is marked with dashed gray lines (Pierce et al., 2017). Western Basin (WB) and Astrolabe Basin (AB) are outlined with thin dashed lines. NVL-Northern Victoria Land; GVL-George V Land; Gl.-glacier.

Sheet extent throughout the Oligocene (Liebrand et al., 2017), although ice-sheet extent during the late Oligocene is still unclear (Roberts et al., 2003; Hauptvogel et al., 2017; Kulhanek et al., 2019; Pollard and DeConto, 2020).

During the early to mid-Miocene (23–14 Ma), large fluctuations in atmospheric CO₂ led to dynamic advance and retreat of the Antarctic ice sheet (Naish et al., 2001; Levy et al., 2016; Gasson et al., 2016; Paxman et al., 2018, 2019b). This was followed by the mid-Miocene climate transition (ca. 14 Ma), when declining atmospheric CO₂ caused Southern Ocean sea-surface temperature cooling and allowed for ice-sheet growth and cold-based ice-sheet conditions (Shevenell et al., 2004; Lewis et al., 2007, 2008; Hauptvogel and Passchier, 2012; Halberstadt et al., 2021). During the mid-Miocene

climate transition, advance and retreat of the Wilkes Subglacial Basin ice sheet are recorded by pulses of ice-rafted debris and offshore sediment wedges (Escutia et al., 2005; Pierce et al., 2017).

During the mid-Pliocene warm period (3.264–3.025 Ma), benthic foraminifera δ¹8O records, offshore Sr and Nd records, and solid earth and ice-sheet modeling suggest that grounded ice in the Wilkes Subglacial Basin retreated hundreds of kilometers inland (Winnick and Caves, 2015; Cook et al., 2013, 2017; Austermann et al., 2015). Following the mid-Pliocene warm period, Ross Sea surface temperatures cooled by ~2.5 °C, and the Antarctic ice sheet grew to extents similar to those of the modern ice sheet (McKay et al., 2012). Ice-sheet modeling, offshore sedimentologic studies, and terrestrial subglacial precipitate studies indicate

that the ice sheet in the Wilkes Subglacial Basin retreated during warm interglacials throughout the Pleistocene (Mengel and Levermann, 2014; Wilson et al., 2018; Blackburn et al., 2020; lizuka et al., 2023).

Reconstructing the Evolution of Subglacial Topography

Topography plays an important role in the growth and stability of an ice sheet, as well as influencing the location of major glacial erosion (Kessler et al., 2008; Jamieson et al., 2008, 2010; Paxman et al., 2020). Additionally, when coupled climateice sheet models use maximum versus minimum Antarctic paleotopography estimates, modeled ice volume for equivalent climate scenarios can vary by

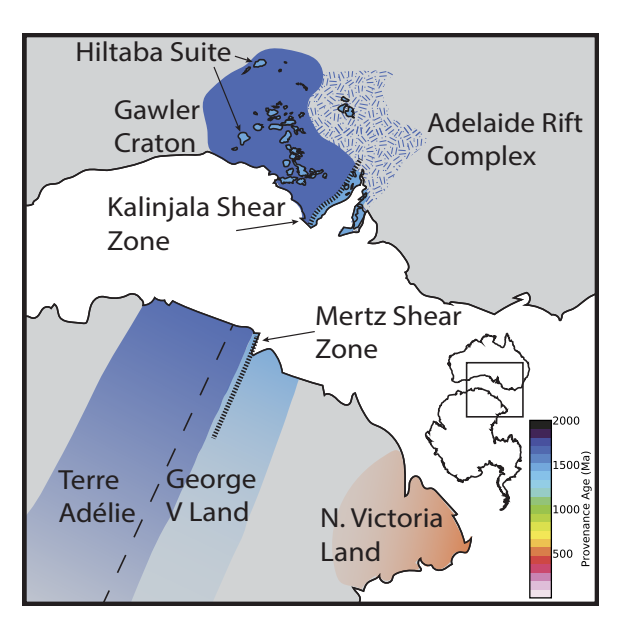


Figure 2. Cartoon showing geologic terranes and inferred correlation of the conjugate margins of Antarctica and Australia (modified from Di Vincenzo et al., 2007; Chapman et al., 2019). Terre Adélie and George V Land are Paleoproterozoic and Mesoproterozoic in age and correlated to the Gawler craton (Naumenko-Dèzes et al., 2020; Duclaux et al., 2007, 2008; Di Vincenzo et al., 2007). Northern Victoria Land is Ediacaran in age (Lamarque et al., 2018).

up to 30% (Wilson et al., 2013; Gasson et al., 2016). Even though paleotopography plays an important role in the way in which we interpret ice-sheet records and model ice-sheet histories, our ability to constrain paleotopographic reconstructions in Antarctica is limited by sparse bedrock data.

The primary data source for existing Antarctic paleotopographic reconstructions is seismic reflection surveys of offshore sediment thickness (e.g., De Santis et al., 1999; Lindeque et al., 2016; Straume et al., 2019; Hochmuth et al., 2020). Once offshore sediment volume is estimated, models of ice-sheet catchments, i.e., areas in which ice flows to a common outlet, are used to redistribute the estimated offshore sediment back onto the continent. When redistributing sediment, large uncertainties in factors such as isostasy, thermal subsidence, sediment compaction, and terrigenous fraction lead to concomitant uncertainties in paleotopographic reconstructions (Paxman et al., 2019a). For the Wilkes Subglacial Basin, total estimates of glacial erosion are further constrained by geomorphic analysis and flexural modeling (Paxman et al. 2018, 2019b), but adding bedrock thermochronology can still significantly reduce model uncertainties by providing bounds for the range of change in topography for Wilkes Subglacial Basin.

Dating dropstones with geochronometers and thermochronometers that encompass a range of closure temperatures (60-800 °C; multimethod dating), and combining these data with a depositional age from the sediment record allow us to constrain the thermal history of a dropstone. Furthermore, the high-temperature thermochronology ages of the dropstone can provide a means to trace the provenance of the dropstone to a likely bedrock source in the continental interior by comparison with the relatively well-known geological history of Wilkes Subglacial Basin. Thus, individual dropstones provide a unique opportunity to use a combination of higher- and lower-temperature thermochronometers (60-800 °C) to constrain the thermal and exhumation history of the subglacial source region through time.

SAMPLES

We sampled 10 dropstones from three Integrated Ocean Drilling Program (IODP) Expedition 318 drill

sites. Table 1 contains a summary of the sampled dropstones. The naming convention represents the depositional epoch of the dropstone followed by its depositional age relative to other dropstones within the epoch, with 1 being the oldest.

Dropstones O-1 and O-2 were deposited during the early Oligocene (30 Ma; Escutia et al., 2011; Tauxe et al., 2012) and were taken from continental shelf site 1360A (Fig. 1, 66.3673°S, 142.7451°E, –506 m). Dropstone O-1 is an ~20-cm-long, potassium feldspar–rich, coarse-grained granite, and O-2 is an ~3.5-cm-long, rounded, potassium feldspar granite.

Dropstones P-1, P-2, P-3, and P-4 were deposited during the Pliocene (ca. 3 Ma), overlapping with the mid-Pliocene warm period, and Pl-1 was deposited during the late Pleistocene or earliest Holocene (IODP Expedition 318 Scientists, 2011a). All Pliocene–Pleistocene dropstones were sampled from continental shelf site 1358B (66.090412°S, 143.31279°E, –510 m). Dropstone P-1 is an ~5-cmlong, subangular, amphibolite clast; P-2 is a slightly angular, ~3-cm-long schist; and P-3 is a rounded ~4-cm-long, fine-grained potassium feldspar granite. Dropstone P-4 is a 14-cm-long, coarse-grained, potassium feldspar-rich granite, and Pl-1 is an ~4-cm-long, rounded, fine-grained, potassium feldspar granite.

From drill site 1356A (63.31023°S, 135.99896°E, –4003 m), located on the transition of the continental rise to the abyssal plain, dropstone O-3 was deposited during the late Oligocene (24 Ma), and dropstones M-1 and M-2 were deposited during the Miocene (14 Ma; Tauxe et al., 2012). Dropstone O-3 is an ~3-cm-long, subangular, fine-grained mafic clast, while M-1 and M-2 are ~4-cm-long, coarse-grained, granodiorite clasts.

METHODS

Sample Preparation

We disaggregated dropstones with a SELF-RAG electric pulse disaggregation device and then wet-sieved disaggregated material into size fractions of <45 μ m, 45–250 μ m, and >250 μ m. Biotite,

TABLE 1. SUMMARY INFORMATION FOR EAST ANTARCTIC DROPSTONES LISTED BY DEPOSITIONAL AGE

Name	IODP drill site	Core	Core section	Interval within core section (cm)	Depositional age (Ma)	Lithology	Provenance age (chronometer)	Dated with chronometers	Interpreted onshore location	
0-1	1360A	5R	1W	20–38	30	K-feldspar-rich medium-grained granite	1720 Ma (U-Pb zircon)	U-Pb zircon, U-Pb apatite, 40Ar/39Ar biotite, AFT, ZHe, AHe	Adélie Land	
0-2	1360A	5R	1W	12–17	30	K-feldspar granite	1730 Ma (U-Pb zircon)	U-Pb zircon, 40Ar/39Ar biotite, AHe	Adélie Land	
O-3	1356A	51R	1W	64–67	24	Fine-grained mafic clast	212–181 Ma (⁴⁰ Ar/ ³⁹ Ar feldspar)	⁴⁰ Ar/ ³⁹ Ar feldspar	Ferrar large igneous province	
M-1	1356A	19R	5W	119–123	14	Granodiorite	1520 Ma (⁴⁰ Ar/ ³⁹ Ar biotite)	U-Pb zircon, 40Ar/39Ar biotite	Adélie Land	
M-2	1356A	19R	5W	109–113	14	Granodiorite	1780 Ma (U-Pb zircon)	U-Pb zircon, 40Ar/39Ar biotite, AHe	Adélie Land	
P-1	1358B	4R	2W	10–14	3	Amphibolite	1740 Ma (⁴⁰ Ar/ ³⁹ Ar hornblende)	⁴⁰ Ar/ ³⁹ Ar hornblende, AHe	Adélie Land	
P-2	1358B	4R	2W	5–8	3	Schist	n/a	U-Pb zircon, AHe	Northern Victoria Land	
P-3	1358B	4R	1W	117–121	3	Fine-grained granite	1880-1150 Ma (⁴⁰ Ar/ ³⁹ Ar biotite)	⁴⁰ Ar/ ³⁹ Ar biotite, AHe	Mertz shear zone	
P-4	1358B	4R	1W	35–50	3	K-feldspar-rich medium-grained granite	1700 Ma (U-Pb zircon)	U-Pb zircon, 40Ar/39Ar muscovite, AHe	Adélie Land	
PI-1	1358B	1R	CC	11–15	0.1-0.01	Fine-grained granite	1530 Ma (U-Pb zircon)	U-Pb zircon, 40Ar/39Ar biotite, AHe	Adélie Land	

Notes: IODP—Integrated Ocean Drilling Program; AFT—apatite fission track; AHe—apatite (U-Th)/He; ZHe—zircon (U-Th)/He.

muscovite, hornblende, apatite, and zircon were then isolated and picked from the 45–250 µm fraction (see Supplemental Material¹).

Thermochronology Analysis

We conducted apatite and zircon U-Pb analysis at the University of Arizona LaserChron Center with laser-ablation–multicollector–inductively coupled plasma–mass spectrometry (LA-MC-ICP-MS) following the methods of Thomson et al. (2012) and Gehrels et al. (2006, 2008), respectively. Stepheating measurements of ⁴⁰Ar/³³Ar biotite and

single-step fusion measurements of ⁴⁰Ar/³⁹Ar biotite, muscovite, feldspar, and hornblende were conducted at Lamont Doherty Earth Observatory's Argon Geochronology for the Earth Sciences laboratory (Supplemental Material). AFT analysis was conducted at the University of Arizona Fission Track Laboratory via the external detector method (Supplemental Material), and (U-Th)/He measurements were conducted at the University of Arizona Radiogenic Helium Dating Laboratory with an Element2 ICP-MS (Supplemental Material). We calculated raw ages using these measurements and applied a polished crystal alpha-ejection correction (Reiners et al., 2007) to derive a corrected (U-Th)/He age.

HeFTy Inverse Modeling

We used HeFTy v2.1.2 for both forward and inverse time-temperature and time-depth modeling (Ketcham, 2005) in order to explore the long-term cooling and exhumation histories recorded by the

dropstones from crystallization to offshore deposition. For the inverse time-temperature modeling, we placed constraint boxes corresponding to the high-temperature chronometer ages and closure temperatures of each dropstone (Supplemental Material) and a constraint box corresponding to cooling to 0 °C by the depositional age of the dropstone, since the time from plucking of the dropstone by a glacier to deposition offshore is nearly instantaneous in the time-scale resolution of HeFTy modeling. The average basal temperature of the East Antarctic Ice Sheet in the Wilkes Subglacial Basin is close to 0 °C (Siegert et al., 2005), as affirmed by the presence of subglacial lakes (Siegert, 2000), and the basal temperatures must be close to the pressure melting point of the glacier in order for bedrock plucking to occur (e.g., Röthlisberger and Iken, 1981).

We ran inverse time-temperature modeling for each dropstone until HeFTy produced 100 good paths or, if no good paths were produced after 200,000 generated paths, until inverse time-temperature

^{&#}x27;Supplemental Material. Contains age data and metadata for all chronometers and HeFTy model inputs and statistics and material including more detailed methods and a discussion on the dispersion of ZHe ages in dropstone O-1. Please visit https://doi.org/10.1130/GEOS.S.25106855 to access the supplemental material, and contact editing@geosociety.org with any questions. Data related to this paper will be housed in the Interdisciplinary Earth Data Alliance data repository (https://doi.org/10.26022/IEDA/112520).

modeling produced 100 acceptable paths. We imposed an AHe age error of 10%–20% to better reflect the intra-dropstone dispersion of AHe ages (Table S7). HeFTy allows a maximum of seven crystal ages for inverse and forward modeling, so we binned ZHe and AHe ages by effective uranium (eU, where [eU] = [U] + 0.235[Th] + 0.0046[Sm]) when more than seven ages were available for a given dropstone (e.g., Murray et al., 2016; Johnson et al., 2017).

After conducting inverse time-temperature modeling, we conducted inverse time-depth modeling using an initial geothermal gradient of 20 °C/km based on modeling of the Antarctic upper mantle and crust (Stål et al., 2020). Due to increasing uncertainty in time-depth modeling as the depth domain increases (HeFTy v2 manual; Supplemental Material), we limited time-depth modeling to depths of 10–17 km over the past 500 m.y. To calculate total exhumation since 34 Ma, we took each time-depth path and linearly interpolated the depth of the dropstone at 34 Ma.

RESULTS

Dropstone 0-1

We dated dropstone O-1 with six different thermochronometers: U-Pb zircon and apatite, 40Ar/39Ar biotite, ZHe, AFT, and AHe (Fig. 3). Cathodoluminescence imagery of a thin section of the dropstone showed zoned growth in apatite crystals, with both apatite crystals concentrated within larger biotite grains (Fig. 3D). U-Pb zircon analysis showed strong discordance with an upper intercept of 1723 ± 9 Ma and a lower intercept of 149 ± 55 Ma (Fig. 3A). We attribute this discordance to Pb loss in partially to highly metamict zircon crystals based on the inverse correlation between percent concordance and eU (Fig. S1; e.g., Mezger and Krogstad, 1997). U-Pb apatite analysis produced an age of 1599 ± 28 Ma. Biotite crystals were dated with 40Ar/39Ar either as single-step fusion or with a step-heating approach. Single-step fusion yielded dates of 1690 ± 5 Ma, 1694 ± 6 Ma, and 1696 ± 3 Ma (Fig. 4). Of five step-heated biotite crystals, all showed evidence of disturbance, with young ages in the initial steps, and two yielded

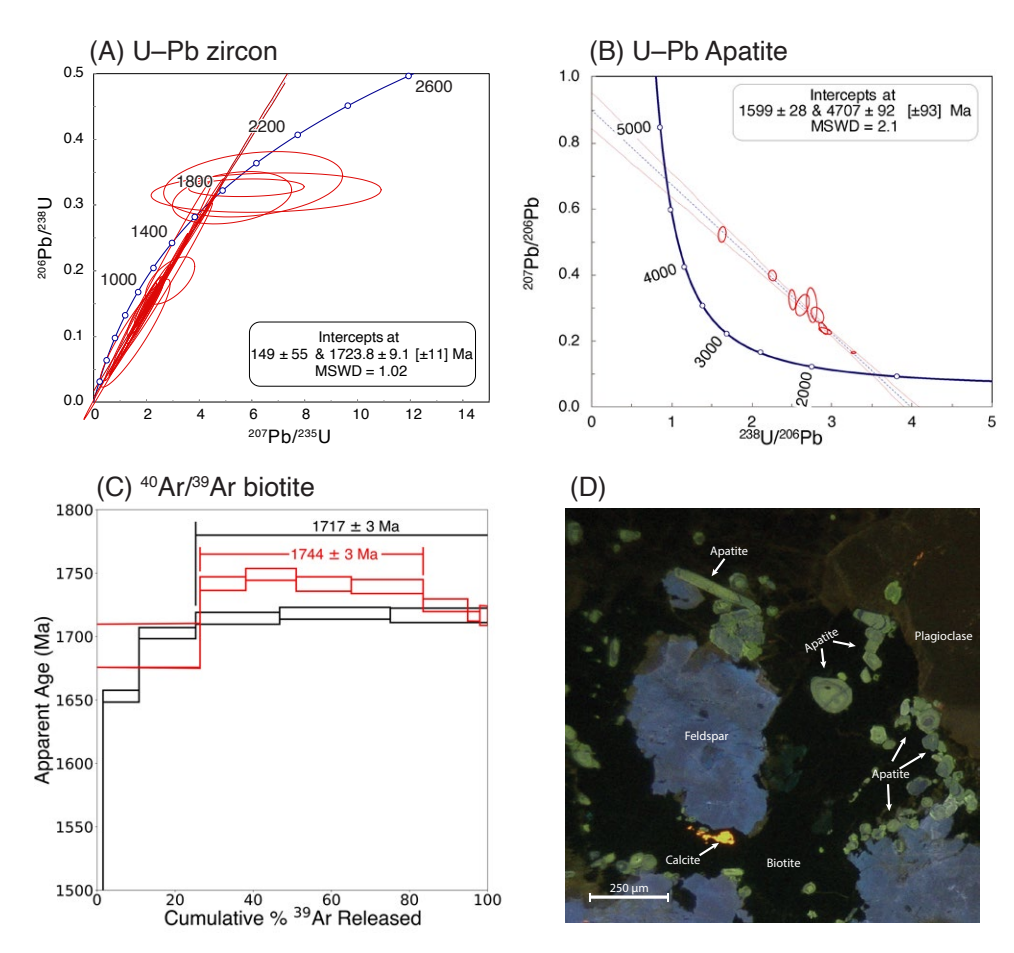


Figure 3. Data from dropstone O-1: (A) U-Pb zircon concordia plot; (B) Tera-Wasserburg plot for U-Pb apatite; (C) 40Ar/39Ar biotite step-heating spectra that yielded plateau ages; and (D) cathodoluminescence image. MSWD—mean square of weighted deviates.

plateau ages of 1716 \pm 1.4 Ma (integrated age 1700 \pm 1.4 Ma) and 1743 \pm 1.3 Ma (integrated age 1726 \pm 3 Ma) (Fig. 3C), while three other crystals produced no plateau but did give integrated ages of 1682 \pm 2 Ma, 1725 \pm 2 Ma, and 1728 \pm 2 Ma (Fig. 4). Although Ar loss at low-temperature steps indicates some alteration or complication within the biotite's history, the similarity of plateau ages to integrated ages suggests that this alteration was minimal and would not alter our provenance or thermal history

interpretations. ZHe single-crystal ages ranged from 614 ± 27 Ma to 1.22 ± 0.02 Ma and showed a strong ZHe age–eU correlation (Fig. 5A). The central AFT age was 238 ± 15 Ma, and the mean track length was 13.77 ± 0.09 µm, with standard deviation of 0.94 µm. The mean c-axis projection-corrected track length (Ketcham et al., 2007) was 14.76 µm, with standard deviation of 0.72 µm. AHe single-crystal ages ranged 444 ± 7 Ma to 365 ± 6 Ma and showed a slightly positive AHe age–eU correlation (Fig. 5B).

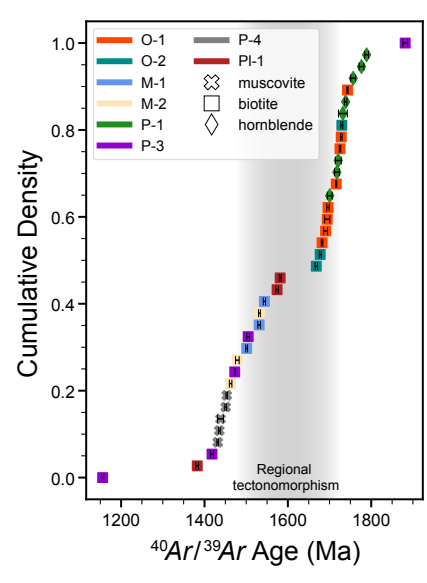


Figure 4. Cumulative density function of all 40 Ar/ 39 Ar ages. Ages from each dropstone are colored as indicated in the legend, and marker shape depicts mineral as indicated in the legend. Error bars show $\pm 2\sigma$ error.

Select apatite crystals were multimethod dated with U-Pb, AFT, and AHe, and these ages are reported in Figure 6. All of these crystals, as well as two double-dated (AFT and AHe) grains, showed AHe ages much older than AFT ages.

Remaining Dropstones

Due to the generally smaller size and lower mineral yields of the other nine dropstones, we dated them with zircon U-Pb, single-step fusion ⁴⁰Ar/³⁹Ar, and single-grain AHe where practical. As indicated by the step heating of biotite from dropstone O-1, there is potential complexity in the biotite history of these dropstones, and single-step fusion dating smooths out some of this complexity; however, for the application of these ages to thermal history and provenance interpretations, these impacts are minimal. Zircon U-Pb results from igneous dropstones O-2, M-2, and P-4 yielded upper-intercept concordant ages of 1800–1700 Ma, whereas granite

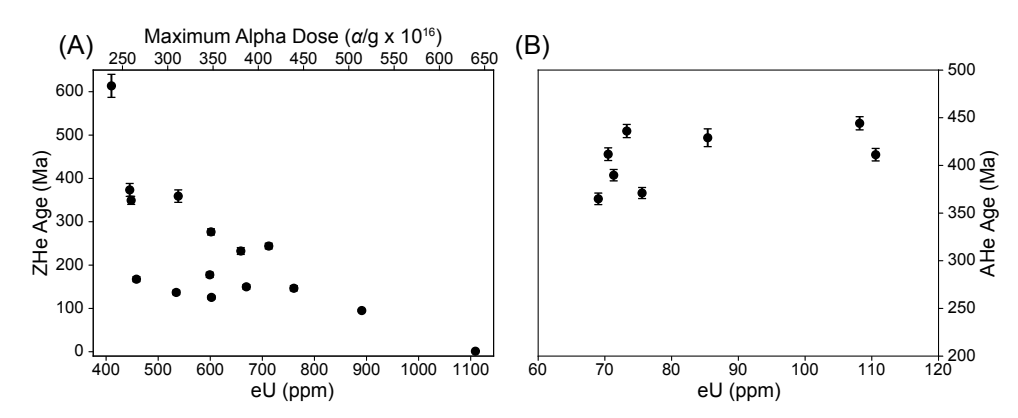


Figure 5. (A) Zircon (U-Th)/He (ZHe) age vs. effective uranium (eU) from dropstone O-1 with 1σ error bars (most are smaller than markers). Maximum alpha dose was calculated with alpha dose accumulation time equal to the difference between each ZHe age and the mean ⁴⁰Ar/³⁹Ar age (Johnson et al., 2017; Nasdala et al., 2005). (B) Apatite (U-Th)/He (AHe) age vs. eU from dropstone O-1 with 1σ error bars.

dropstone PI-1 showed a concordant age of 1531 Ma (Fig. 7). Dropstone P-2, a schist, yielded a detrital zircon U-Pb age distribution with peaks at 500 Ma and 1000 Ma from 21 dated grains (Fig. 7). The 40Ar/39Ar biotite, muscovite, and hornblende showed prominent populations at ca. 1500 Ma (dropstones M-1, M-2, P-4) and ca. 1700 Ma (dropstones O-1, P-1, O-2; Fig. 4). Although these chronometers contain different closure temperatures, we plotted them together given the similarity in offshore age populations seen across 40Ar/39Ar hornblende and 40Ar/39Ar biotite (Pierce et al., 2014). Dropstone P-3 contained age dispersion of up to ~700 Ma with ages ranging from 1881 to 1155 Ma, while dropstone PI-1 contained age dispersion of up to 200 Ma with ages ranging from 1581 to 1382 Ma. Single-grain AHe ages in three of the other dropstones (O-2, P-2, and P-3) showed age ranges similar to that of sample O-1, from ca. 479 to 311 Ma; M-2 showed a relatively narrow spread from 199 to 176 Ma, PI-1 showed a larger range of 388–113 Ma, all at relatively low eU, P-1 yielded two ages at 97 Ma and 26 Ma, and P-4 yielded two ages at 53 Ma and 30 Ma (Figs. 8B and 8C). Several of these ages showed weak positive correlations with eU and/or effective spherical radius. The AHe age results of the thermochronology measurements are summarized in Table 2.

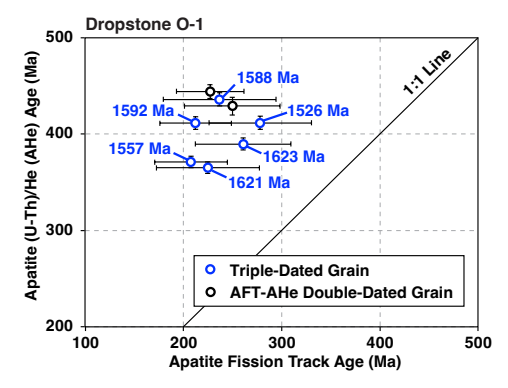
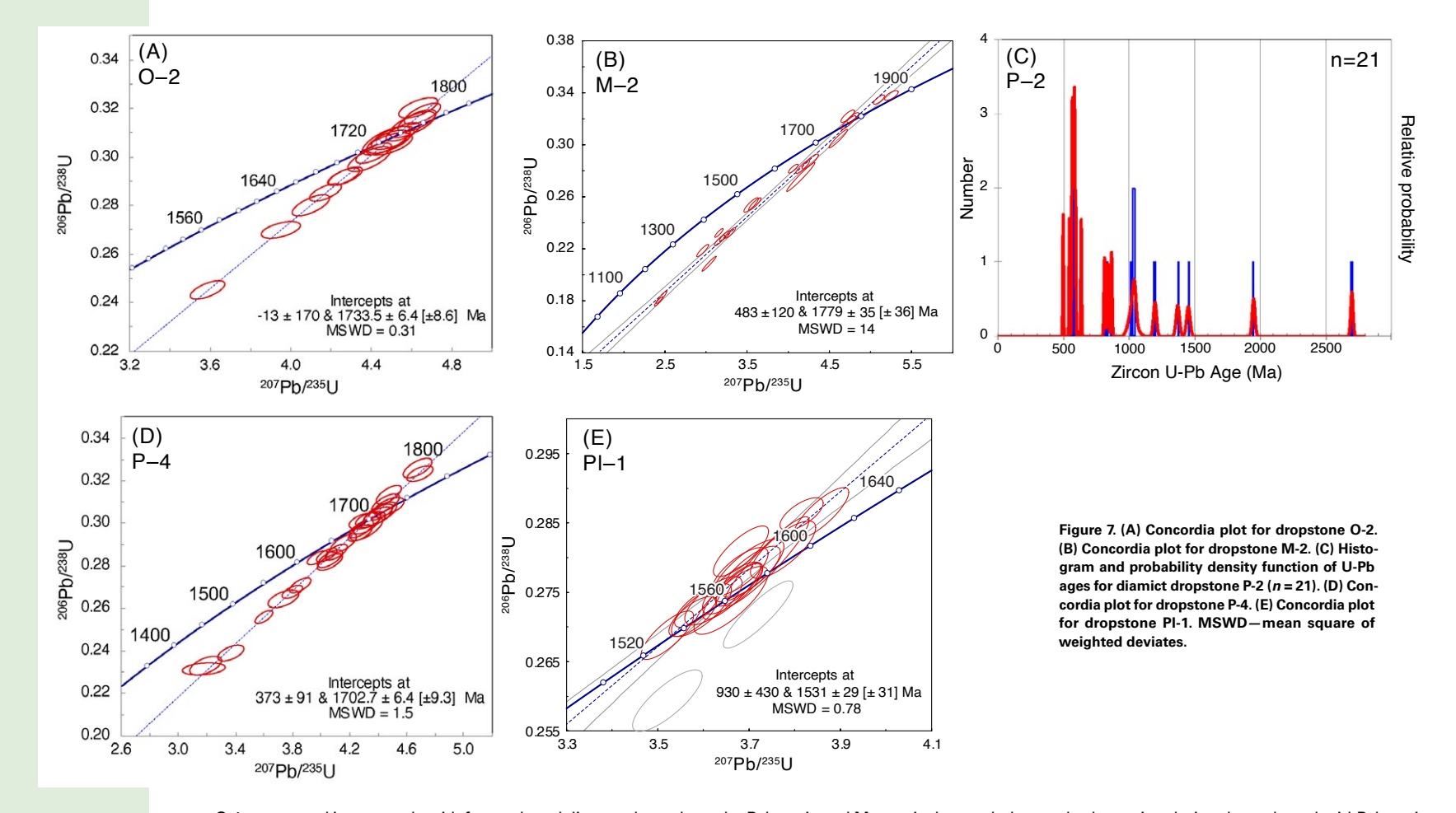


Figure 6. Plot of apatite fission-track (AFT) vs. apatite (U-Th)/He age for apatite crystals that were double dated from dropstone O-1. Crystals for which U-Pb ages were also measured are outlined in blue, and ages are given.

DISCUSSION

HeFTy Inverse Modeling

We present HeFTy inverse modeling for dropstones O-2, M-2, P-1, P-2, P-3, P-4, and Pl-1. Due to the complex and extensive data set of dropstone



O-1, we treated it separately with forward modeling. Inverse modeling for dropstones M-2, P-1, P-2 and P-3 yielded paths with good fits to the measured data, while dropstones O-2, P-4, and Pl-1 produced only acceptable-fit paths for both time-temperature and time-depth modeling (Fig. 9). The timing and magnitude of time-temperature and time-depth models for a given dropstone were in generally good agreement when a constant geothermal gradient of 20 °C/km was used to transform time-temperature paths to time-depth space, except for dropstone O-2. The majority of time-temperature paths for dropstone O-2 (Fig. 9A, purple) showed slow cooling rates

throughout the Paleozoic and Mesozoic that cooled to 0 °C by ca. 100 Ma, with some paths that showed rapid cooling during the Paleozoic that cooled to 0 °C by as early as ca. 400 Ma. Time-depth paths for O-2 (Fig. 9A, orange) showed rapid cooling in the early Paleozoic (500–400 Ma) that then transitioned to slow or very slow cooling from ~60 °C to 0 °C. If the oldest AHe age of dropstone O-2 is excluded, time-temperature inverse modeling showed good-fit paths, as opposed to acceptable paths, of rapid exhumation during the early Paleozoic (Fig. S2).

Inverse time-depth and time-temperature paths for dropstones O-2, P-2, and P-3 showed rapid cooling

and exhumation during the early and mid-Paleozoic (500–350 Ma), while dropstones P-1 and P-4 showed rapid cooling and exhumation during the late Cenozoic. Dropstones M-2 and Pl-1 showed a mix of slow, constant cooling through the Paleozoic as well as some paths predicting rapid cooling and denudation occurring during the Mesozoic (ca. 200 Ma; Fig. 9).

We attempted HeFTy inverse modeling for dropstone O-1; however, the combination of its large thermochronology data set, AFT central age that is significantly younger than AHe ages, strong ZHe age–eU relationship, and its long 1.7 b.y. thermal history led to computationally expensive HeFTy

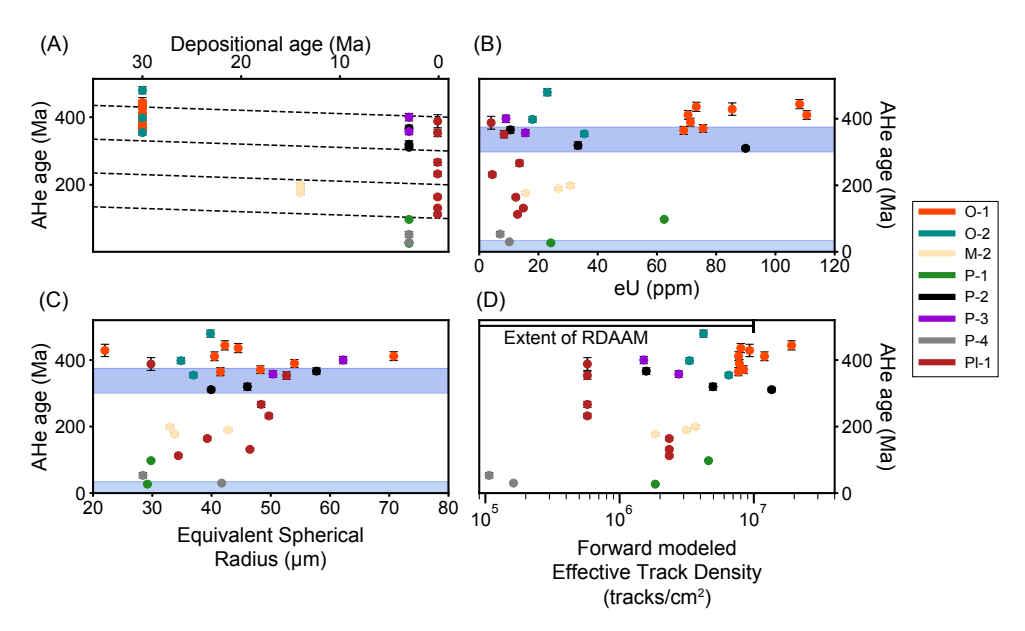


Figure 8. Apatite (U-Th)/He (AHe) ages compared with other information about the dropstones. (A) AHe age vs. depositional age. Dashed lines show constant lag time, which is the time between closure of AHe and deposition. (B) AHe age vs. eU. (C) AHe age vs. equivalent spherical radius. (D) AHe age vs. modeled effective track density using the best-fit time-temperature path from the HeFTy forward model (radiation damage accumulation and annealing model [RDAAM]). For all panels, AHe ages from the same dropstone are colored the same, and error bars shown with ±20 error.

modeling with strict conditions that did not produce any "good" or "acceptable" time-temperature paths. As a result, we used HeFTy forward modeling and compared forward-modeled AFT ages and track lengths, ZHe ages, AHe ages, and ZHe age-eU relationships with our data set to produce a preferred thermal history that most closely predicted the AHe ages, AFT age and track lengths, and ZHe ages and age-eU relationship of this dropstone.

Forward Thermal History Modeling of Dropstone 0-1

In theory, multimethod dating of dropstone O-1 with numerous thermochronologic systems provides greater constraints on its possible thermal histories. However, not all the thermochronometers pointed to mutually consistent ranges of time-temperature histories (e.g., Fig. 5). In particular, the ZHe and AHe systems, together with other thermochronometers, pointed to contrasting histories that were not possible to reconcile with currently available kinetic models of the systems. Dropstone O-1's inverted AHe and AFT ages can be easily modeled with a nonmonotonic cooling history (Flowers et al.,

TABLE 2. SUMMARY OF THERMOCHRONOMETER AGES FOR EACH EAST ANTARCTIC DROPSTONE

Dropstone	U-	Pb	⁴⁰ Ar/ ³⁹ A	ır		(U-Th)/He			
name	Zircon	Apatite	Mineral	Age (Ma)				Zircon	Apatite
	Age ± 1σ (Ma)	Age ± 1σ (Ma)	•		Age ± 1σ (Ma)	Mean track length (μm)	Standard deviation (µm)	Age (Ma)	Age (Ma)
O-1	1723 ± 9	1599 ± 28	Biotite	1728–1690	238 ± 15	13.77	0.94	614–1	444–365
0-2	1733 ± 6		Biotite	1729-1668					479-354
O-3			Plagioclase-feldspar	212-181					
M-1			Biotite	1543-1501					
M-2	1779 ± 35		Biotite	1531-1462					199–176
P-1			Hornblende	1788-1700					97, 26
	800-500								
P-2	1300-1000								366-311
	2700-1400								
P-3			Biotite	1881–1155					400-358
P-4	1703 ± 6		Muscovite	1453-1431					53, 30
PI-1	1531 ± 29		Biotite	1581–1382					388–113

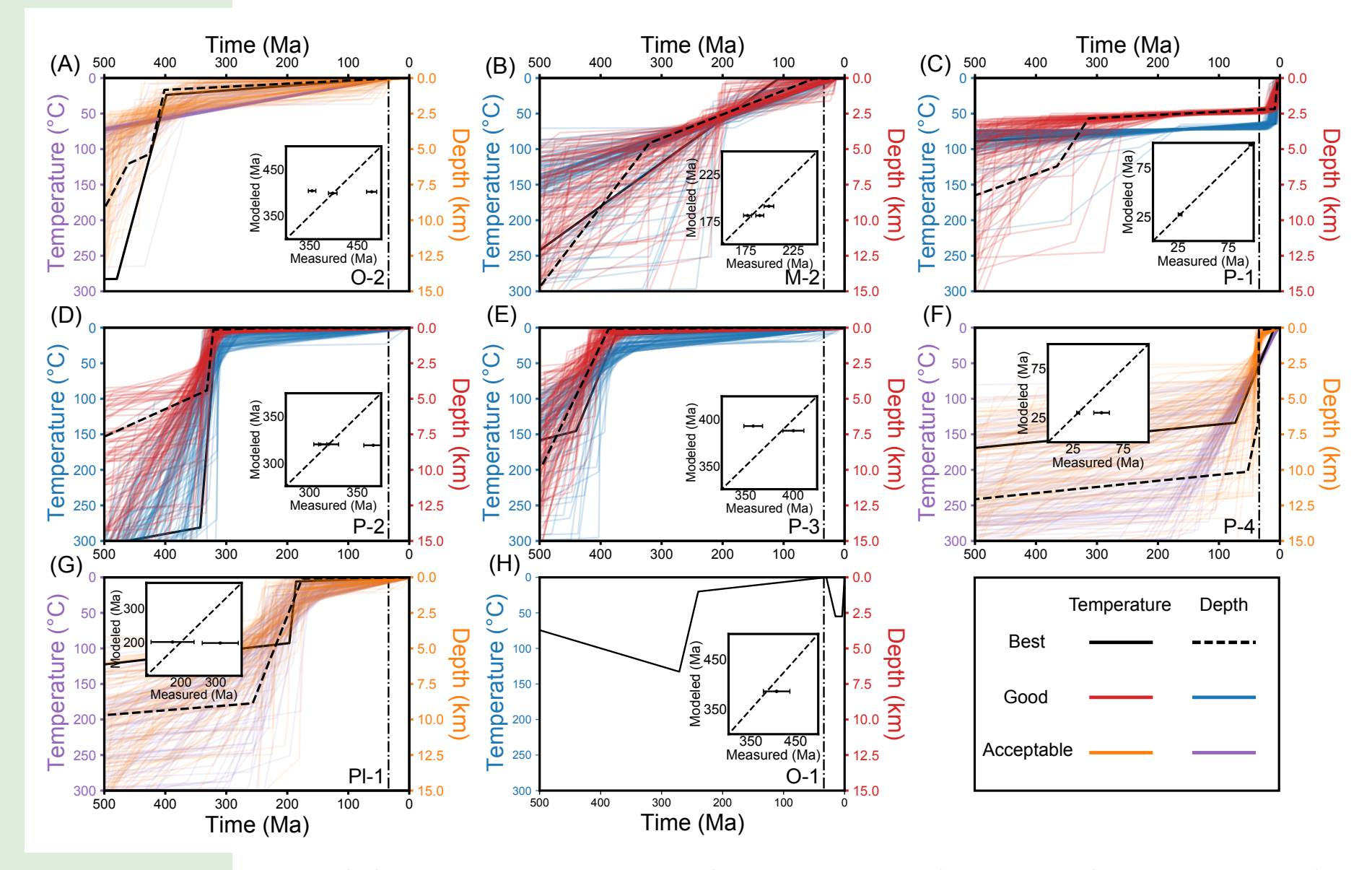


Figure 9. (A–G) Subset view of HeFTy inverse time-temperature paths (blue—good fit, purple—acceptable fit) and inverse time-depth (red—good fit, orange—acceptable fit) from 500 to 0 Ma. For clear viewing, only the 100 best time-temperature and 100 best time-depth paths are drawn. Insert shows comparison of HeFTy modeled time-temperature apatite (U-Th)/He (AHe) ages and measured AHe ages. (H) Subset view of proposed thermal history for dropstone O-1 from 500 to 0 Ma. Dash-dot line marks 34 Ma, indicating the onset of Cenozoic glaciation in Antarctica.

2009; Reiners et al., 2017, their fig. 11.25), involving a long residence at temperatures below the partial annealing zone for AFT (120–60 °C) followed by a relatively short (~10–50 m.y.) reheating episode to ~100 °C and subsequent cooling during the Permian-Triassic (ca. 250 Ma; Fig. 10A). Similarly, the strong ZHe age—eU relationship and AFT age and track lengths can be reproduced by a long residence at temperatures below the partial annealing zone for zircon fission tracks (ZFTs; 330–262 °C; Yamada et al., 2007) followed by a longer reheating period (100–200 m.y.) at ~120 °C from the early to mid-Paleozoic (ca. 500 Ma) to the Permian-Triassic boundary (ca. 250 Ma) with rapid cooling occurring during the Early Triassic (Fig. 10B).

The discrepancy in the duration of reheating required by the ZHe age-eU relationship and nonresetting of the AHe ages could be explained by insufficient representation of the ZHe system (discussed in the following section), or by insufficient representation of annealing within the AHe system. The radiation damage accumulation and annealing model (RDAAM) models radiation damage annealing with a fission-track annealing model, but alpha decay radiation damage has been shown to be more resistant to annealing than fission tracks (Willett et al., 2017). Apatite crystals in O-1 likely sustained greater radiation damage than the apatite used to calibrate RDAAM (Fig. 8D). Therefore, to reconcile the ZHe, AFT, and AHe data sets, we used a simple approach and reduced the AFT annealing model r_{mr0} parameter used in RDAAM (Ketcham et al., 1999) to 0.5 (from 0.83) to simulate an increased resistance to annealing (Fox et al., 2017; Winn et al., 2017), which allows the AHe to not fully reset when undergoing the longer-duration reheating required to produce the ZHe age-eU relationship. We altered r_{mr0} only for dropstone O-1, since it was the only dropstone that could not be modeled with the default RDAAM parameters.

Given the spread in ZHe ages and the need to adjust RDAAM to create a thermal history that matched the measured AHe ages, the thermal history for dropstone O-1 is difficult to predict confidently. Our final preferred thermal history was achieved by forward modeling a thermal history defined by five segments (Fig. 11):

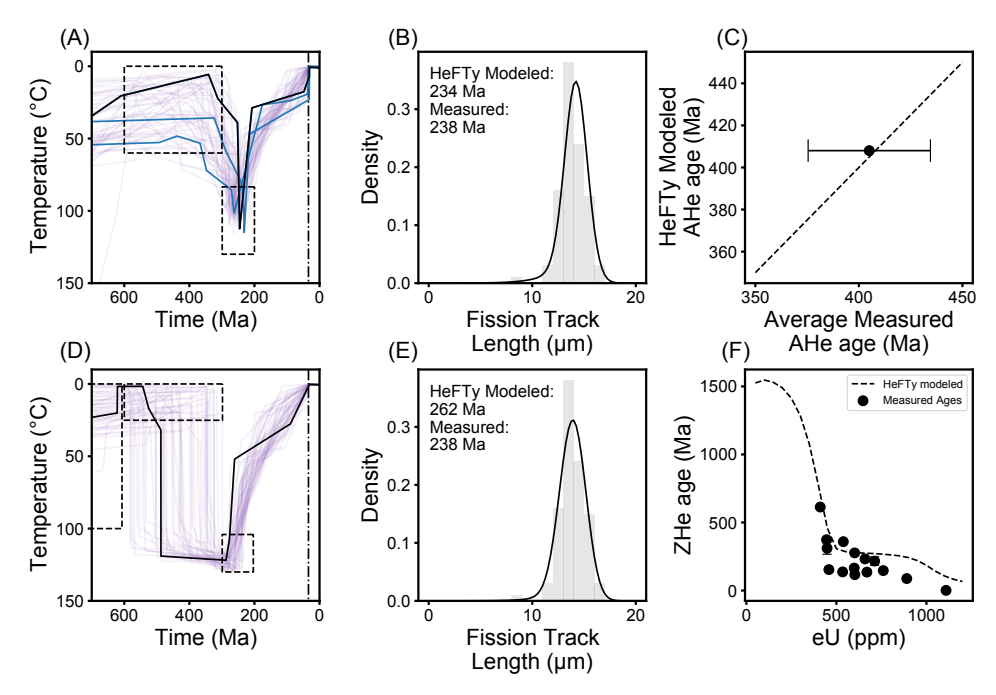


Figure 10. (A) Subset view of HeFTy inverse time-temperature paths for dropstone O-1 apatite (U-Th)/He (AHe) and apatite fission-track (AFT) data (blue—good fit, purple—acceptable fit) from 700 to 0 Ma. Dash-dot line marks 34 Ma. (B) Histogram of measured α-axis projected AFT lengths and probability density function of HeFTy forward-modeled α-axis projected apatite fission-track lengths based on AHe and AFT inverse modeling. Modeled and measured AFT ages are reported in the top-left corner. (C) Forward-modeled HeFTy age plotted against average AHe age with 1 standard deviation error bar. (D–E) Same as A–B but for inverse modeling with dropstone O-1 zircon (U-Th)/He (ZHe) and AFT data. (F) Measured and modeled ZHe age—effective uranium (eU) relationships. Black dots are measured values. Forward modeled ZHe age—eU relationship is based on the thermal history in panel A with radius of 50 μm.

- Rapid cooling to 100 °C within 100 m.y. of crystallization.
- (2) Slow cooling throughout the Proterozoic and into the Paleozoic (1600–500 Ma).
- (3) reheating to 130 °C during the Paleozoic (500–270 Ma).
- (4) Rapid cooling during the late Paleozoic and Early Triassic to 20 °C, followed by slow cooling that brought dropstone O-1 to 0 °C at the time of its deposition offshore.
- (5) After deposition, reheating to a peak temperature of 55 °C at 15 Ma that was held until 4 Ma, when the dropstone cooled to ~0 °C by present day.

The thermal history shows rapid cooling within 100 m.y. of crystallization due to the similarity of U-Pb zircon, U-Pb apatite, and 40Ar/39Ar biotite ages despite their closure temperatures of 900–800 °C for U-Pb zircon (Williams and Ellis, 1997), 550–450 °C for U-Pb in apatite (Cherniak et al., 1991), 500 °C for 40Ar/39Ar hornblende, and 300 °C for 40Ar/39Ar biotite (Grove and Harrison, 1996). Final cooling during this phase to 100 °C was necessary because the strong ZHe age–eU relationship (Fig. 5A) and AHe-AFT age inversion require a long residence below the ZFT and AFT partial annealing zones to accumulate radiation damage (Yamada et al., 2007; Reiners and Brandon, 2006).

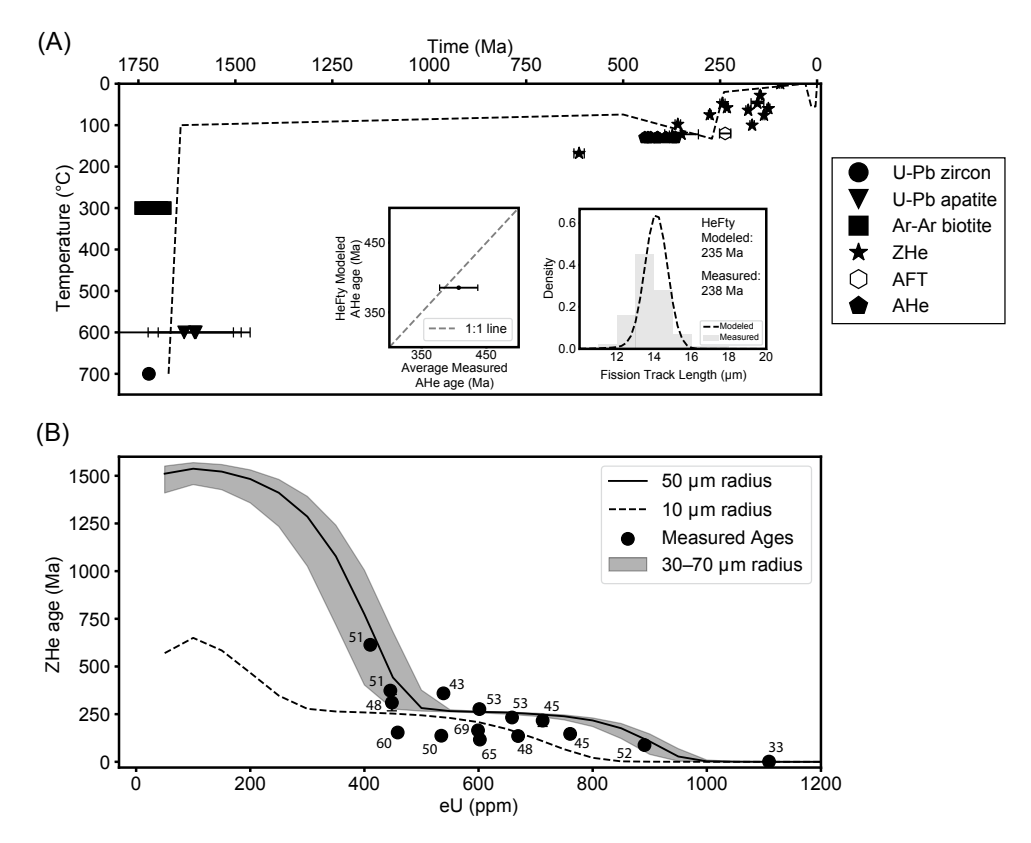


Figure 11. (A) Proposed thermal history for dropstone O-1. Left inset shows forward-modeled HeFTy age plotted against average apatite (U-Th)/He (AHe) age with 1 standard deviation error bar. Right inset shows histogram of measured c-axis projected apatite fission-track lengths and probability density function of HeFTy forward-modeled c-axis projected apatite fission-track lengths. Modeled and measured apatite fission-track (AFT) ages are reported in the top right corner. (B) Measured and modeled zircon (U-Th)/He (ZHe) age-effective uranium (eU) relationships. Black dots are measured values and are labeled with their crystal radius. Forward-modeled ZHe age-eU relationship is based on the thermal history in panel A with radius of 50 µm (black line), with range between 70 µm and 30 µm (gray), and with radius of 10 µm (black dashed).

The slow cooling of segment 2 allowed radiation damage to accumulate in regions of zircon crystals with high eU. This radiation damage allowed zircon and apatite crystals to lose He when the dropstone reheated after 500 Ma, before the onset of rapid cooling to 20 °C during segment 3 ca. 250 Ma. We speculate that this reheating was related to burial by sediments produced by erosion during and after the Ross orogeny immediately to the west of the present-day Wilkes Subglacial Basin (Federico et

al., 2006; Lisker and Olesch, 2003; Lisker, 2002; Di Vincenzo et al., 2007; Goodge, 2007). The presence of sedimentary basins of this age is supported by modeled depths to magnetic basement ranging from 2.5 to 7.5 km within the Wilkes Subglacial Basin (Aitken et al., 2014). The rapid cooling ca. 250 Ma aligns with AFT data from George V Land and ZHe and AHe data from the Bunger Hills in the western Wilkes Land sector of East Antarctica (~100°E), which had been proposed to be associated with

extension of the Wilkes Subglacial Basin (Lisker and Olesch, 2003; Maritati et al., 2020). After rapid Paleozoic–Triassic cooling, the dropstone slowly cooled until it was plucked from the bedrock surface and deposited offshore at 30 Ma.

Following deposition, our preferred thermal history includes reheating to ~55 °C, indicating postdepositional burial by ~1.5 km of Oligocene and Miocene sediment. This reheating more accurately reproduces the young, high-eU ZHe ages and anneals modeled AFT track lengths to lengths similar to those measured. Such burial is supported by seismic reflection profiles of the glacial sediment stratigraphy of the continental shelf close to site U1360, which indicates significant Oligocene to early Miocene sediment accumulation below an unconformity believed to mark the Miocene climatic optimum (17–14.8 Ma; Escutia et al., 2005; IODP Expedition 318 Scientists, 2011b; Sauermilch et al., 2019).

Figure 11 shows our preferred thermal history for dropstone O-1, the forward-modeled ZHe age-eU relationship predicted by zircon RDAAM (ZRDAAM; Guenthner et al., 2013) compared to the measured ZHe age and eU concentration of each grain, and a comparison of the predicted versus measured average AHe age and AFT track length distribution. The ZHe data exhibit a scattered inverse ZHe age-eU relationship, with larger ZHe age dispersion among crystals with lower eU (Fig. 11B). When our preferred thermal history (Fig. 11A) is forward modeled using ZRDAAM of Guenthner et al. (2013), predicted ZHe ages match the upper bound of the ZHe age-eU relationship, but the model does not explain the dispersion of lower-eU ZHe ages.

Our preferred forward model thermal history produces AHe ages that match measured ages when $r_{\rm mrm0}$ is reduced to 0.5 (Fig. 11A). The AHe ages of O-1 are notably old, ~150 m.y. older than the AFT ages and older than most of the ZHe ages. Our forward model produces a central AFT age (235 Ma) similar to the measured central age (238 \pm 15 Ma). The forward-modeled AFT track lengths (with mean c-axis projection track length of 14.28 \pm 0.64 μ m) are similar to the measured c-axis projected track lengths of 14.76 \pm 0.72 μ m (Fig. 11A).

Low-eU ZHe Age Dispersion of Dropstone 0-1

The dispersion of lower-eU ZHe ages of dropstone O-1 may be caused by U-Th zonation (e.g., Schaltegger et al., 1999), which can lead to an incorrect alpha ejection correction (Guenthner et al., 2013), but it may also lead to zones of high and low radiation damage that are undetected in bulkcrystal average eU values. Zones of high eU may experience a high alpha dose (>2 × $10^{18} \alpha/g$) that lowers the closure temperature (Guenthner et al., 2013), leading to a younger crystal ZHe age than expected given the measured bulk eU. Additionally, these zones of high eU may lead to mixing of multiple diffusion domains of differing size within zircon grains, possibly as a consequence of microfracturing created from expansion related to metamictization of high-U and high-Th zones (Reiners et al., 2002). We were unable to model accurately the potential impacts of these factors in HeFTy owing to a lack of information on the nature of zoning in each individual zircon crystal. However, to explore the extent to which lower-eU ZHe age dispersion can be explained by these processes, we conducted exploratory eU end-member and diffusion domain size end-member analysis (Fig. 12; Supplemental Material).

Low-eU end members with eU >200 ppm create mixing lines that pass through the upper bounds of the measured ZHe data, although this does not explain the younger portion of the age dispersion. However, a mixing line using a low-eU end member with eU of 50 ppm with a predicted ZHe age of 1535 Ma does bracket the lower parts of the measured data. A low-eU end-member domain with fixed eU of 300 ppm and equivalent sphere radius (ESR) of 10 µm, which has been measured in highresolution He and eU maps (Danišík et al., 2017), also creates a mixing line that brackets the lower bounds of the ZHe data cloud (Fig. S6B). This suggests that the dispersion in ZHe ages can likely be explained by some combination of low/high-eU zonation and/or multiple diffusion domains with variable ESR due to metamictization fracturing or perhaps different growth zones within zircon crystals behaving as individual diffusion domains. However, more research into the behavior of radiation damage zonation and its effects on He diffusion in zircon is needed.

Wilkes Subglacial Basin Thermal History

We constructed three generalized thermal histories representative of the measured dropstones from the Wilkes Subglacial Basin by combining high- and low-temperature thermochronologic ages with HeFTy inverse time-temperature modeling. Our generalized thermal history contains a common Proterozoic cooling history that splits into three groups during the Paleozoic (Fig. 13). All samples show rapid cooling to 300 °C or cooler by 1500 Ma, followed by slow cooling from 1500 to 500 Ma (with potential reheating during 1300-1000 Ma; Fig. 12A, red shading). Slow cooling throughout the Proterozoic is likely a simplification of the cooling histories for all dropstones excluding dropstone O-1, and our ages do not preclude cooling and reheating occurring between 0 °C and 300 °C for dropstones O-2, M-3, P-3, P-4, and PI-1 and 0-600 °C for dropstone P-2 throughout the Proterozoic due to the closure temperatures of biotite, muscovite, and hornblende. The ZHe, AFT, and AHe ages of dropstone O-1, however, allow us to constrain slow cooling across this interval. Following 500 Ma, we divided

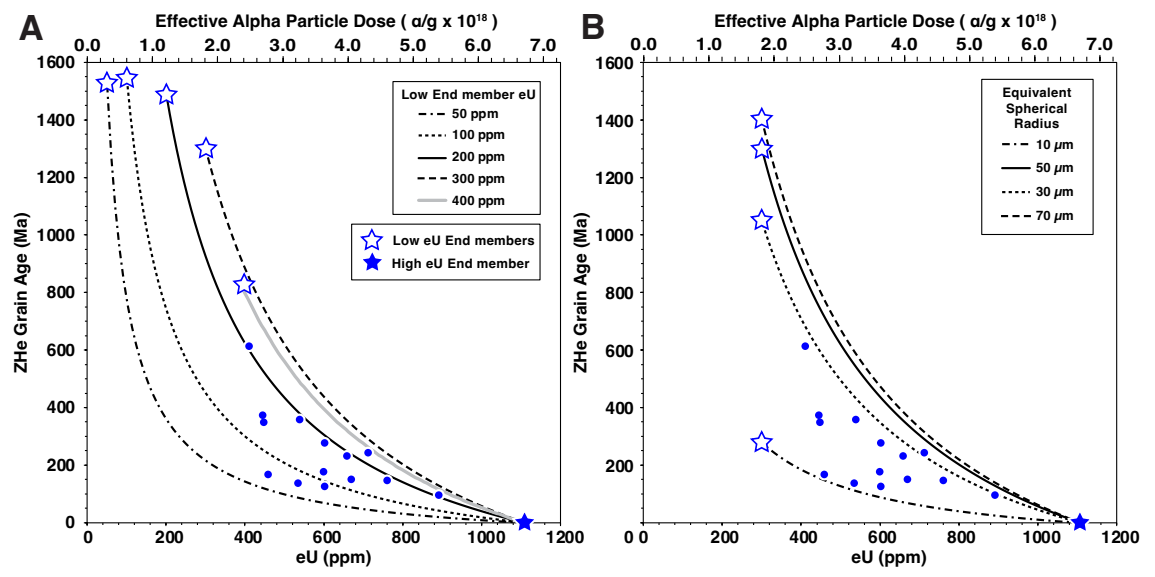


Figure 12. (A) End-member mixing of high-eU and low-eU zones within a zircon crystal. Blue dots are measured zircon (U-Th)/He (ZHe) ages for dropstone O-1. Mixing lines for mixing between multiple low-effective uranium (eU), high-age end members (50, 100, 200, 300, and 400 ppm) with a common high-eU, low-age end member (1109 ppm) are shown. All zones assume a radius of 50 µm. (B) The effect of zone radius on the mixing of high-eU and loweU zones within a single zircon crystal. We held the eU value of the low-eU (300 ppm) and high-eU (1109 ppm) end members constant, but varied the radius of the eU zones (70, 50, 30, 10 μm).

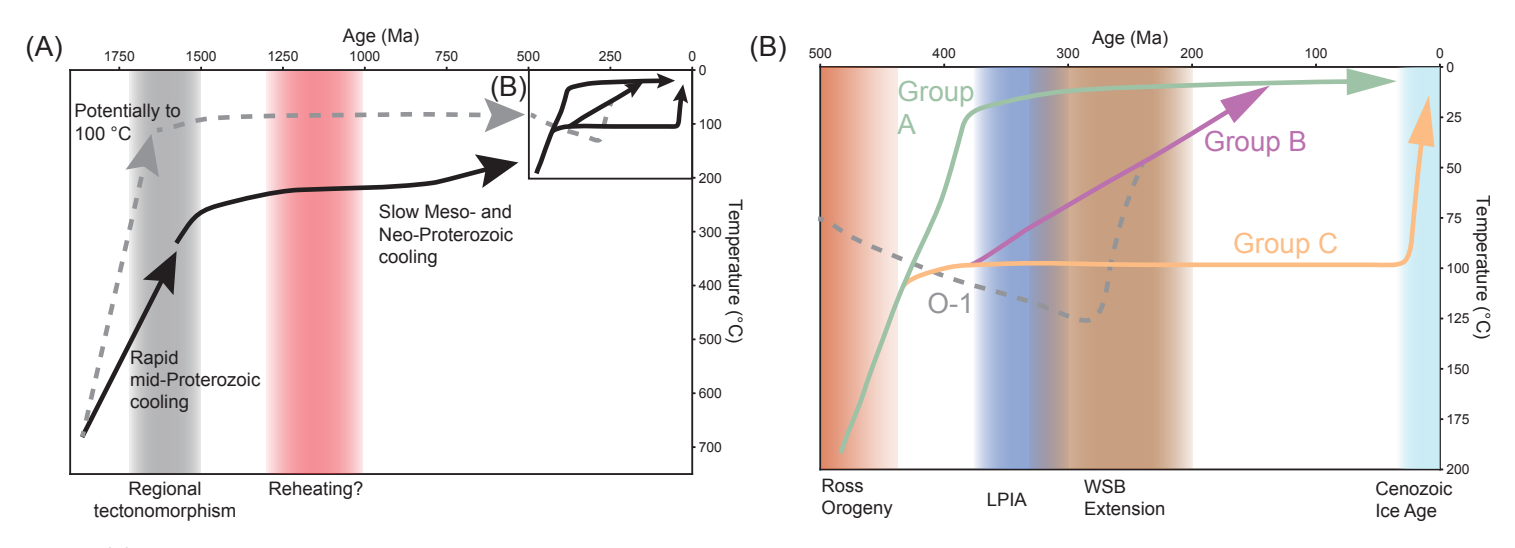


Figure 13. (A) Schematic diagram depicting generalized thermal histories of Wilkes Subglacial Basin and Terre Adélie. Gray dashed arrows show dropstone O-1, while black arrows show all other dropstones. (B) Close-up view of 500–0 Ma. Arrows show cooling histories of group A (green; dropstones O-2, P-2, and P-3), group B (purple; dropstones M-2 and Pl-1), group C (orange; dropstones P-1 and P-4), and O-1 (gray, dashed). Shading show range of ages for the Ross orogeny (red), late Paleozoic ice age (LPIA, blue), Wilkes Subglacial Basin extension (WSB extension, brown), and Cenozoic ice age (cyan).

the Paleozoic cooling histories into three groups: group A (dropstones O-2, P-2, P-3), which rapidly cooled between 500 Ma and 350 Ma to 20–0 °C; group B (dropstones M-2 and Pl-1), which cooled at intermediate rates between 350 Ma and 180 Ma to 20–0 °C; and group C (dropstones P-1 and P-4), which slowly cooled from the Paleozoic (ca. 400 Ma) to the Eocene-Oligocene boundary (34 Ma), after which group C rapidly cooled to 0 °C.

Rapid cooling from crystallization to temperatures cooler than 300 °C by 1500 Ma is constrained by the U-Pb zircon and 40Ar/39Ar biotite ages of dropstones O-1, O-2, M-2, P-4, and Pl-1 and is consistent with known tectono-thermal events in the Adélie craton and Mertz shear zone ceasing ca. 1500 Ma (Di Vincenzo et al., 2007; Naumenko-Dèzes et al., 2020). Cooling of dropstone O-1 to 100 °C is required by accumulation of the radiation damage in zircon and apatite needed to produce a strong ZHe age—eU relationship and inverted AHe ages older than AFT ages. Exploratory HeFTy inverse modeling showed that cooling to 100 °C, as proposed for dropstone O-1, is possible for all other dropstones (Fig. S5); however,

since these dropstones were not dated with AFT and ZHe, we can only constrain cooling to temperatures lower than 300 °C by 1500 Ma, i.e., the closure temperature represented by the biotite 40Ar/39Ar age. Slow cooling from 1500 Ma to 450 Ma is suggested by best-fit HeFTy inverse time-temperature paths (Fig. S15). Potential Grenville-aged (1300–1000 Ma) reheating leading to partial resetting or recrystallization is suggested by the range in 40Ar/39Ar biotite ages for dropstones P-3 and PI-1 (Fig. 4), and evidence for fault reactivation during this time is seen in the Gawler craton (Foster and Ehlers, 1998). The Mesoproterozoic interval of the dropstones' thermal histories is relatively unconstrained during this time compared to other time periods, although significant reheating to metamorphic temperatures sufficient to fully reset these thermochronometers can be ruled out.

Reheating during the Paleozoic (500–270 Ma) is only recorded by the AFT, ZHe, and AHe ages from dropstone O-1. However, exploratory HeFTy inverse time-temperature modeling of all other dropstones that forced reheating during this time similar to

that proposed for dropstone O-1 showed that AHe ages from the other dropstones can be produced with reheating from 500 to 270 Ma similar in magnitude to dropstone O-1, although with variable timing (Fig. S5).

Rapid early and mid-Paleozoic cooling (500-380 Ma) is constrained by the mid-Paleozoic AHe ages (Fig. 8) of dropstones O-2, P-2, and P-3 and HeFTy inverse time-temperature modeling (Fig. 9). This rapid cooling event slightly predates the modeled cooling of AFT and AHe ages from the Adélie craton and George V Land associated with the late Paleozoic ice age (Rolland et al., 2019; Voisine et al., 2020) as well as AFT ages from George V Land marking extension of the Wilke Subglacial Basin (Lisker and Olesch, 2003). From thermal modeling of dropstones O-2, P-2, and P-3, we interpret ~100 °C of cooling throughout the early to mid-Paleozoic (Figs. 9A, 9D, and 9E). This magnitude of cooling is similar to that interpreted by Rolland et al. (2019), Voisine et al. (2020), Lisker (2002), and Lisker and Olesch (2003) from coastal bedrock outcrops, but with slightly older initiation of cooling.

The old AHe ages of dropstones O-2, P-2, and P-3 lead to HeFTy inverse time-temperature paths that cool during the early to mid-Paleozoic (500-400 Ma), prior to the cooling seen by previous Adélie craton low-temperature thermochronometry work (Rolland et al., 2019; Voisine et al., 2020), but similar to the ca. 500 Ma cooling recorded in glacial erratics deposited near Byrd glacier interpreted to be associated with either the Pan-African orogeny and configuration of Gondwana or the more local Ross orogeny (Fitzgerald and Goodge, 2022). These older AHe ages of dropstones O-2, P-2, and P-3 may suggest initial influence from uplift associated with the Ross orogeny, which then transitioned into denudation and uplift associated with the late Paleozoic ice age (Rolland et al., 2019; Voisine et al., 2020). Regardless of the cause, our ice-rafted dropstones appear to record the influence from a slightly older Paleozoic cooling event, which is not captured via moraine and bedrock exposure sampling methods located on the eastern margin of Wilkes Subglacial Basin (Rolland et al., 2019; Voisine et al., 2020).

Inverse time-temperature modeling of dropstones M-2 and PI-1 suggested intermediate to rapid rates of cooling throughout the late Paleozoic and early Mesozoic. The timing of this cooling is similar to interpreted extensional tectonic-driven cooling and exhumation in the Lambert Rift (Lisker et al., 2003), George V Land (Lisker and Olesch, 2003), and Bunger Hills (Maritati et al., 2020), which has been interpreted to represent intracontinental rifting (Maritati et al., 2020) that would have impacted Wilkes Subglacial Basin. Glacial erratics deposited in the Transantarctic Mountains also record Jurassic (ca. 180 Ma) cooling associated with Gondwana rifting (Fitzgerald and Goodge, 2022). The Mesozoic and Paleozoic AHe ages of dropstones M-2 (199-176 Ma) and Pl-1 (388-113 Ma) paired with their HeFTy inverse models (Figs. 9B and 9G) suggest that portions of Wilkes Subglacial Basin were impacted by these extensional events.

If dropstones M-1 and Pl-1 record late Paleozoic and Mesozoic extension within Wilkes Subglacial Basin, the earlier cooling histories of dropstones O-2, P-2, and P-3 suggest that the widespread intracontinental rifting proposed by Maritati et al. (2020) was not uniform throughout Wilkes Subglacial Basin.

Alternatively, it is also possible that dropstones O-2, P-2, and P-3 were buried with sediment during this time, causing partial resetting of the AHe system, similar to dropstone O-1, which experienced cooling during the Mesozoic. However, our current data set does not allow us to make such claims.

One important finding provided by our dropstone data is that the young AHe ages from dropstones P-1 (26 Ma) and P-4 (30 Ma) record previously unknown rapid post-Eocene cooling in Wilkes Subglacial Basin indicative of >2 km of exhumation of crystalline bedrock since 34 Ma. Previous records of local glacial denudation of this magnitude in cratonic East Antarctica have been reported from the Lambert graben (Thomson et al., 2013) and Dronning Maud Land (Sirevaag et al., 2021). Onshore low-temperature thermochronometry in Terre Adélie suggests limited Cenozoic erosion, i.e., <1.5 km of erosion since 30 Ma (Rolland et al., 2019). The youngest reported onshore AHe ages are older than 100 Ma. In contrast, our new single-grain AHe analyses from dropstones P1 and P3 included single-grain ages younger than 30 Ma, providing new evidence for significant localized glacial incision to depths of at least 2 km in some parts of the Wilkes Subglacial Basin.

Dropstone Provenance

Previous work detailing the provenance of offshore detrital records and onshore detrital moraine deposits (Goodge et al., 2010; Pierce et al., 2011, 2014; Licht and Hemming, 2017) can be compared to the limited onshore bedrock exposures (Cooper et al., 1985; Ménot et al., 2007; Di Vincenzo et al., 2007; Naumenko-Dèzes et al., 2020), allowing us to confidently assign general provenance of dropstones to terranes in Wilkes Subglacial Basin with some confidence. However, we were not able to pinpoint exact outcrop locations, and we cannot rule out that these dropstones may have originated from unmapped, ice sheet-covered, geologic terranes. Dropstones O-1, O-2, M-1, M-2, P-1, P-4, and PI-1 contain provenance signatures found in Terre Adélie. Dropstones O-1, O-2, M-2, and P-4 contain Paleoproterozoic (1780-1600 Ma) U-Pb

zircon ages that are similar to those of the Adélie craton (Ménot et al., 2007; Naumenko-Dèzes et al., 2020). Dropstone P-4 contains ⁴⁰Ar/³⁹Ar biotite ages that coincide with the Mertz shear zone (Fig. 4; Di Vincenzo et al., 2007); however, granulite crust local to the shear zone is Neoarchean in age (Naumenko-Dèzes et al., 2020) and older than the Paleoproterozoic U-Pb zircon ages of dropstone P-4. Dropstone P-4 may have originated from a glaciated region of Terre Adélie that intersects with the Mertz shear zone (Fig. 1); however, this is speculative.

The 1491 ± 6 Ma ⁴⁰Ar/³⁹Ar biotite age of dropstone M-2 matches well with the 1525 ± 5 Ma 40Ar/39Ar biotite age of dropstone M-1. Given their similar granodiorite lithology and similar depositional depth in drill core site 1356A, we interpret that dropstone M-1 also originated from the Adélie craton. The U-Pb zircon age of 1531 ± 29 Ma for dropstone PI-1 and the average 40Ar/39Ar biotite age of 1512 ± 5 Ma match previous ages of the Hiltaba granite suite in the Gawler craton (1514 +32 Ma; Cooper et al., 1985), which has been correlated to the Adélie craton (Peucat et al., 2002; Goodge et al., 2017) and would be expected to be located to the west of the Mertz shear zone (Fig. 2); however, they are ~50 m.y. younger than recently published ages (ca. 1595-1575 Ma; Chapman et al., 2019). Amphibolite dropstone P-1 has an average 40Ar/39Ar hornblende age of ca. 1700 Ma, which matches hornblende ages from amphibolite outcrops directly west of the Mertz shear zone (Di Vincenzo et al., 2007; Naumenko-Dèzes et al., 2020). This ca. 1700 Ma terrane extends inland and underlies the upstream sections of the Mertz Glacier (Fig. 2).

Dropstone P-3, a fine-grained granite, has a median biotite ⁴⁰Ar/³⁹Ar age of 1472 ± 2 Ma with ages ranging from 1881 to 1155 Ma. It may have originated from Neoarchean granulite crust located proximal to the Mertz shear zone that underwent ⁴⁰Ar/³⁹Ar resetting ca. 1500 Ma (Naumenko-Dèzes et al., 2020). Dropstone P-3 was not dated with U-Pb zircon; however, the spread of ⁴⁰Ar/³⁹Ar ages (Fig. 4) is potential evidence of variable partial resetting of the ⁴⁰Ar/³⁹Ar system caused by the Mertz shear zone or Grenville-aged (1300–1000 Ma) local fault reactivation similar to that seen in the Gawler craton (Foster and Ehlers, 1998).

The detrital zircon U-Pb age populations of dropstone P-2, a schist, show that it likely originated from the metasedimentary sequences of northern Victoria Land (Fig. 7D). However, since only 21 zircon crystals were dated from dropstone P-2, the exact terrane from which this dropstone originated is difficult to determine, but the higher abundance of ca. 500 Ma ages relative to ca. 1000 Ma ages, presence of Archean ages, elevated Th/U (Fig. S3), and its lithology indicate that it likely originated from the Millen schist belt of northern Victoria Land (Estrada et al., 2016).

A thin section of dropstone O-3 shows it to be a plagioclase-bearing basalt (Fig. S4). Additionally, its youngest ⁴⁰Ar/³⁹Ar plagioclase feldspar age (181 Ma) is consistent with the age of the Ferrar large igneous province (Fleming et al., 1997). The two older ⁴⁰Ar/³⁹Ar ages (201 Ma and 212 Ma) are also similar to some feldspar K/Ar ages associated with the Ferrar large igneous province (Fleming et al., 1997). Therefore, we interpret dropstone O-3 as originating from the Ferrar large igneous province.

Implications for the Cenozoic Topographic Evolution of Wilkes Subglacial Basin

The thermochronologic ages and thermal history models we present here provide new constraints on post-34 Ma glacial exhumation in the Wilkes Subglacial Basin and allow us to estimate total exhumation since 34 Ma for each dropstone and by extension, its source bedrock. We produced a range of modeled exhumation since 34 Ma for each dropstone by interpolating the depth at 34 Ma for all HeFTy time-depth paths (Figs. 9 and 14A) and interpreted glacial erosion as the cause of this topographic change, since the Wilkes Subglacial Basin has been relatively tectonically stable over this time period (e.g., Maritati et al., 2020). We then compared our findings to local low-temperature thermochronology studies (Rolland et al., 2019; Voisine et al., 2020) and a model of Antarctica-wide erosion since 34 Ma (Paxman et al., 2019a).

Six of our dropstones recorded median erosion of less than 500 m since 34 Ma (Fig. 14A). Based on the low number of samples, we cannot

generalize these exhumation magnitudes across the whole Wilkes Subglacial Basin and the Adélie craton. However, the Paleozoic AHe ages and HeFTy inverse modeling of dropstones O-1, O-2, P-2, and P-3 contribute to the growing evidence that the interior of East Antarctica has been largely tectonothermally stable since the late Paleozoic despite uplift of the Transantarctic Mountains, potential intracontinental rifting, and Cenozoic glaciation (Cox et al., 2010; Tochilin et al., 2012; Thomson et al., 2013; Rolland et al., 2019; Maritati et al., 2020; Voisine et al., 2020; Fitzgerald and Goodge, 2022).

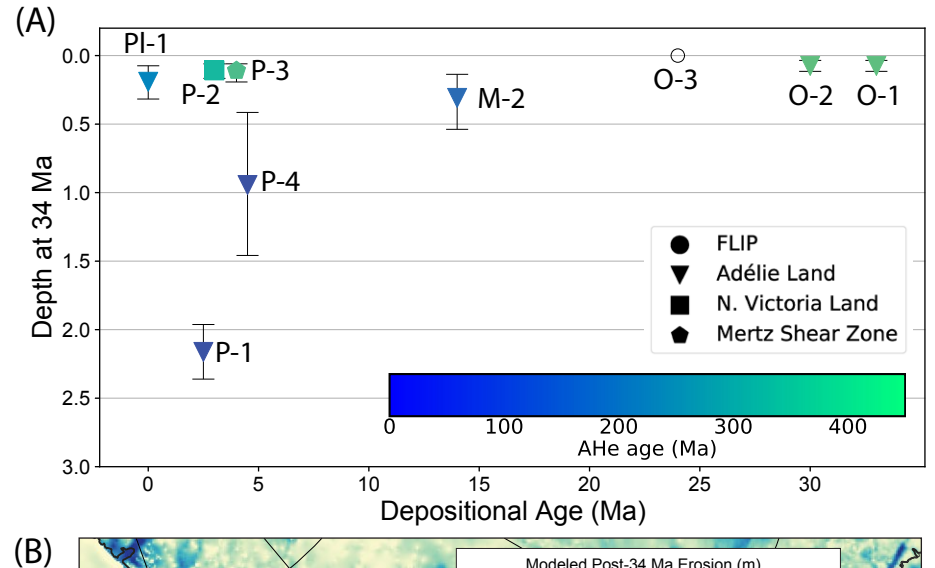
Although the majority of our dropstones record <500 m of erosion since 34 Ma, two of the dropstones indicate significant magnitudes of local exhumation in the Wilkes Subglacial Basin since ca. 34 Ma, with dropstone P-1 recording median total exhumation of +2 km and P-4 recording median total exhumation of ~1 km (~2 km since 40 Ma). Both dropstones P-1 and P-4 provide new independent evidence for ~2 km of cooling and localized glacial erosion in the Wilkes Subglacial Basin since 34 Ma (Fig. 14A). The provenance of dropstone P-4 indicates origins from the Adélie craton, with ca. 1450-1430 Ma ⁴⁰Ar/³⁹Ar biotite ages indicating some influence by the Mertz shear zone, suggesting a source within the Western Basin of the Wilkes Subglacial Basin (Fig. 14B). Dropstone P-1, with its ca. 1700 Ma 40 Ar/39 Ar hornblende ages, indicates it was not affected by later ca. 1500 Ma resetting along the Mertz shear zone, suggesting a source within the undeformed parts of the Adélie craton interior, perhaps from the base of the Mertz Glacier subglacial trough, placing a lower limit on the amount of localized glacial erosion (~2 km) in the Mertz subglacial trough since 34 Ma (Fig. 14B).

The Western Basin and interior of the Mertz shear zone record relatively slow present-day ice-surface velocities of 10°–10¹ m/yr (Fig. 14C), suggesting that past ice-sheet flow conditions distinct from those of present day would be required to produce the magnitudes of erosion we infer from our data. We consider that this fast erosion may have occurred during the Oligocene and Miocene when the Antarctic ice sheet was more dynamic and erosive (Young et al., 2011; Thomson et al., 2013; Pierce et al., 2017; Paxman et al., 2019b; Jamieson et al., 2023).

Rolland et al. (2019) dated samples collected along the Terre Adélie coast with AFT and AHe. The AFT ages ranged from 317 to 251 Ma (mean track lengths of 13.15–14.37 μm), while single-grain AHe ages ranged from 362 to 122 Ma. Best-fit HeFTy inverse paths based on AFT data suggest maximum total exhumation of ~1–1.5 km since 34 Ma. However, the range of good-fit paths does not preclude samples reaching the surface as early as the Cretaceous. Voisine et al. (2020) dated 14 moraine boulders on the Terre Adélie coast with AFT. These AFT ages ranged from 345 to 231 Ma (mean track lengths of 11.18–12.78 μm), and HeFTy inverse modeling suggested exhumation since 34 Ma of <1.5–2 km.

Paxman et al. (2019a) reconstructed Antarctica topography at 34 Ma and then estimated total erosion since 34 Ma by comparing the 34 Ma reconstruction to modern-day Bedmap2 subglacial topography (Fretwell et al., 2013; see also Fig. 14B). The methods to produce the 34 Ma reconstruction were outlined in detail by Paxman et al. (2019a) and included the flexural isostatic response to unloading of the modern ice-sheet load and changes in the geometry of the water load, removal of post-34 Ma volcanic edifices, adjustments for plate motion and thermal subsidence related to the West Antarctic rift system, and erosional restoration estimated using sediment thicknesses derived from offshore seismic reflection data and corrected for sediment compaction and nonterrigenous sediment sources, where estimates of glacial erosion were divided into a spatially uniform component and selective erosion limited to valleys and troughs. This methodology applied by Paxman et al. (2019a) did not, however, account for constraints on total erosion derived from offshore or onshore thermochronology, and therefore the results of this work and others (e.g., Cox et al., 2010; Tochilin et al., 2012; Thomson et al., 2013; Rolland et al., 2019; Voisine et al., 2020) provide an independent comparison to their modeled output.

Specific to Wilkes Subglacial Basin, Paxman et al. (2019a) predicted ≥2 km of erosion in the Astrolabe and Western Basins, similar to our estimates based on HeFTy inverse modeling of dropstone Pl-1. However, estimates of erosion under Mertz Glacier



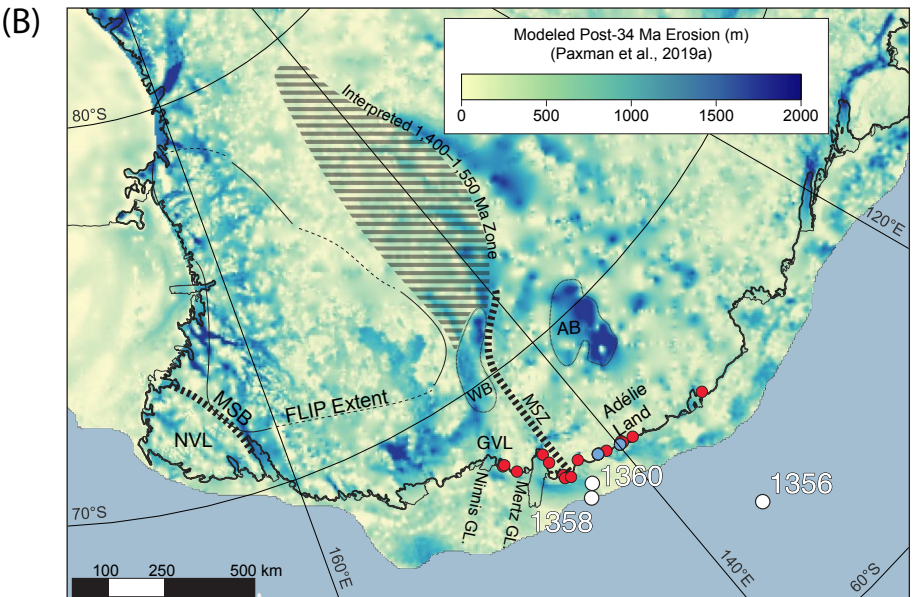
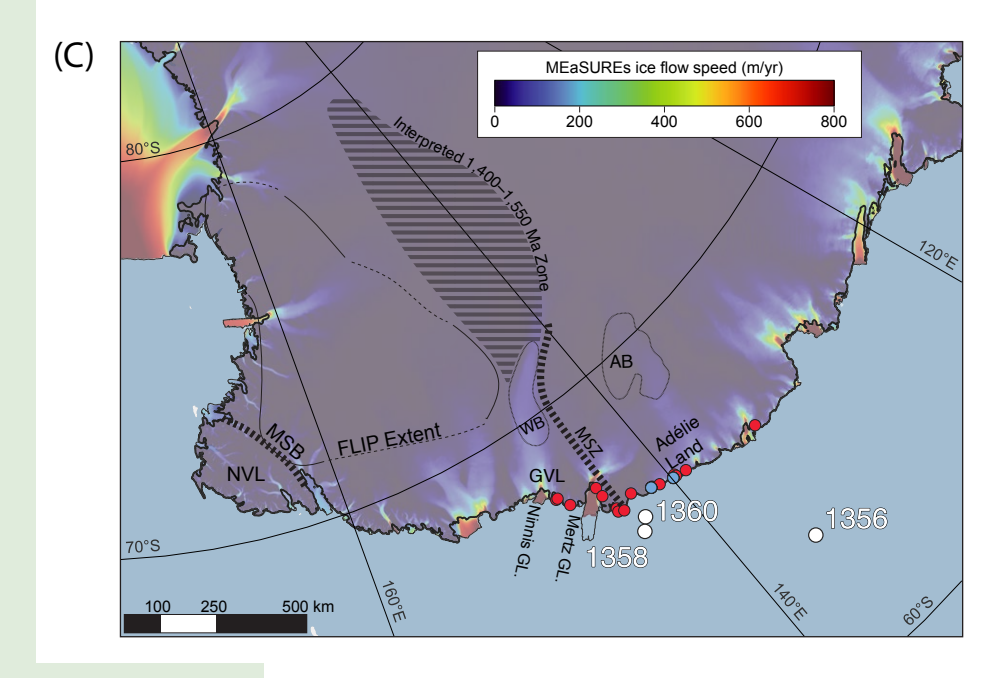


Figure 14. (A) Modeled depth of each dropstone at 34 Ma. Marker shows median depth, and error bars show $\pm 1\sigma$. Markers are colored by representative apatite (U-Th)/He (AHe) age (either average or youngest AHe age). Marker style corresponds to their interpreted provenance terrane. (B) Modeled erosion since 34 Ma from Paxman et al. (2019a, their fig. 5a). (C) MEaSUREs ice flow speed (Rignot et al., 2011). NVLnorthern Victoria Land; MSB-Millen schist belt; FLIP-Ferrar large igneous province; MSZ-Mertz shear zone; WB-Western Basin; AB-Astrolabe Basin; GL.-glacier; GVL-George V Land. Red and blue circles mark locations of on-land low-temperature thermochronology ages from Rolland et al. (2019) and Voisine et al. (2020), respectively.



are 1-2 km (Paxman et al., 2019a), which are slightly below our estimate of +2 km based on HeFTy inverse modeling of dropstone P-4. Reconstructed total erosion estimates for most of the Wilkes Subglacial Basin are primarily less than 1 km, with less than 500 m in much of Terre Adélie (Paxman et al., 2019a; see also Fig. 14B). This agrees with six of our dropstones, which record <500 m of erosion since 34 Ma (Fig. 14A), but it is below erosion estimates based on coastal AFT data (Rolland et al., 2019; Voisine et al., 2020). This discrepancy could arise due to assumptions made by Paxman et al. (2019a) in their quantification of erosion, and the fact that uniform surface lowering across Antarctica is not well constrained for the past 34 m.y. However, work in neighboring Aurora Subglacial Basin suggests the highlands have experienced little erosion since 34 Ma (Jamieson et al., 2023). Additionally HeFTy inverse modeling of coastal data does not preclude smaller magnitudes of Cenozoic erosion less than 1.5 km (Rolland et al., 2019; Voisine et al., 2020).

Our findings also support the idea that some of the deep trenches and basin features in the Wilkes Subglacial Basin formed through glacial erosion (Paxman et al., 2019a), as opposed to forming through tectonic activity (Lisker and Olesch, 2003; Cianfarra and Salvini, 2016; Cianfarra and Maggi, 2017), because the basin has been tectonically stable throughout the late Cenozoic. This is further supported by our finding that younger AHe ages were only found in dropstones deposited during the Pliocene, after the Antarctic ice sheet was dynamically eroding throughout the Oligocene and early Miocene (Paxman et al., 2019a).

CONCLUSION

Our study presents an application of multimethod dating of offshore ice-rafted dropstones to constrain the thermal and exhumation history of the Wilkes Subglacial Basin and Adélie craton. Multimethod dating of dropstones offers several benefits over the common practice of dating single detrital mineral grains; it permits the combined use of high-temperature geochronometers and lowertemperature thermochronometers to constrain the source region of the dropstone by comparing high-temperature geochronometer ages with known geology from sparse outcrops, offshore detrital provenance records, and the geology of Australia. It also allows acquisition of high-quality low-temperature thermochronology data from multiple grains, providing the means to conduct inverse thermal history modeling using multiple lowtemperature thermochronometers from those same dropstones, resulting in a detailed record of the exhumation history of the source. By dating the icerafted dropstones using multiple methods, we were able to show that large-magnitude erosion in Wilkes Subglacial Basin was likely localized to sections of the Mertz Glacier subglacial trough and Adélie craton, including potentially the Western Basin, which have experienced ~2 km of localized Cenozoic glacial erosion. We were able to demonstrate that the source bedrock of most of the dropstones remained within 0-500 m of the surface since the Paleozoic or Mesozoic (400-200 Ma), implying very low erosion rates in the Wilkes Subglacial Basin over this time, as also recorded in other parts of East Antarctica (Cox et al., 2010; Tochilin et al., 2012; Thomson et al., 2013; Rolland et al., 2019; Maritati et al., 2020; Fitzgerald and Goodge, 2022). The abundance of knowledge gained from only 10 ice-rafted dropstones is a testament to the effectiveness of multimethod dating when applied to ice-rafted dropstones in discerning the evolution of the hidden Antarctic geology and topography and portends the important role it can play in future work.

ACKNOWLEDGMENTS

This work was supported by National Science Foundation Office of Polar Program awards 1443565 (Hemming), 1443556 (Thomson and Reiners), 1043572 (Licht), and 0944489 (Hemming and Williams). Uttam Chowdhury and Arizona University He Laboratory staff assisted with (U-Th)/He analysis. University of Arizona LaserChron Center Staff assisted with U-Pb zircon and apatite analysis. Thanks go to Troy Rasbury for providing cathodoluminescence images and helpful discussion. Thanks also go to Cody Randel, Connor Watkins, and Jennifer Castaneda for aiding in sample preparation. This work could not have been done without Integrated Ocean Drilling Program (IODP) Expedition 318 and Expedition 318 scientists. Thanks go to IODP core repository curators for providing additional samples and correspondence for identifying dropstones and to Guy Paxman for providing post-34 Ma median modeled erosion data.

We appreciate the Lamont Doherty Earth Observatory Earth Intern Program and the University of Arizona Antarctichron/ Chronothon workshops for providing opportunities for undergraduate research. This work benefited from conversations with Christine Siddoway and Bailey Nordin. We thank Maria Laura Balestrieri, Yann Rolland, two anonymous reviewers, and Science Editor Andrea Hampel for comments that improved the manuscript.

REFERENCES CITED

- Aitken, A.R.A., Young, D.A., Ferraccioli, F., Betts, P.G., Greenbaum, J.S., Richter, T.G., Roberts, J.L., Blankenship, D.D., and Siegert, M.J., 2014, The subglacial geology of Wilkes Land, East Antarctica: Geophysical Research Letters, v. 41, no. 7, p. 2390–2400, https://doi.org/10.1002/2014GL059405.
- Austermann, J., Pollard, D., Mitrovica, J.X., Moucha, R., Forte, A.M., DeConto, R.M., Rowley, D.B., and Raymo, M.E., 2015, The impact of dynamic topography change on Antarctic ice sheet stability during the mid-Pliocene warm period: Geology, v. 43, no. 10, p. 927–930, https://doi.org/10.1130 /G36988.1.
- Blackburn, T., Edwards, G.H., Tulaczyk, S., Scudder, M., Piccione, G., Hallet, B., McLean, N., Zachos, J.C., Cheney, B., and Babbe, J.T., 2020, Ice retreat in Wilkes Basin of East Antarctica during a warm interglacial: Nature, v. 583, no. 7817, p. 554–559, https://doi.org/10.1038/s41586-020-2484-5.
- Boger, S.D., 2011, Antarctica—Before and after Gondwana: Gondwana Research, v. 19, no. 2, p. 335–371, https://doi .org/10.1016/j.gr.2010.09.003.
- Burgess, S.D., Bowring, S.A., Fleming, T.H., and Elliot, D.H., 2015, High-precision geochronology links the Ferrar large igneous province with Early Jurassic ocean anoxia and biotic crisis: Earth and Planetary Science Letters, v. 415, p. 90–99, https:// doi.org/10.1016/j.epsl.2015.01.037.
- Burton-Johnson, A., Black, M., Fretwell, P.T., and Kaluza-Gilbert, J., 2016, An automated methodology for differentiating rock from snow, clouds and sea in Antarctica from Landsat 8 imagery: A new rock outcrop map and area estimation for the entire Antarctic continent: The Cryosphere, v. 10, no. 4, p. 1665–1677, https://doi.org/10.5194/tc-10-1665-2016.
- Chapman, N.D., Ferguson, M., Meffre, S.J., Stepanov, A., Maas, R., and Ehrig, K.J., 2019, Pb-isotopic constraints on the source of A-type suites: Insights from the Hiltaba Suite-Gawler Range volcanics magmatic event, Gawler craton, South Australia: Lithos, v. 346, https://doi.org/10.1016/j.lithos 2019 105156
- Cherniak, D.J., Lanford, W.A., and Ryerson, F.J., 1991, Lead diffusion in apatite and zircon using ion implantation and Rutherford backscattering techniques: Geochimica et Cosmochimica Acta, v. 55, no. 6, p. 1663–1673, https://doi.org /10.1016/0016-7037(91)90137-T.
- Cianfarra, P., and Maggi, M., 2017, Cenozoic extension along the reactivated Aurora fault system in the East Antarctic craton: Tectonophysics, v. 703, p. 135–143, https://doi.org/10.1016/j.tecto.2017.02.019.
- Cianfarra, P., and Salvini, F., 2016, Origin of the Adventure Subglacial Trench linked to Cenozoic extension in the East Antarctic craton: Tectonophysics, v. 670, p. 30–37, https:// doi.org/10.1016/j.tecto.2015.12.011.

- Colleoni, F., De Santis, L., Montoli, E., Olivo, E., Sorlien, C.C., Bart, P.J., Gasson, E.G., Bergamasco, A., Sauli, C., Wardell, N., and Prato, S., 2018, Past continental shelf evolution increased Antarctic ice sheet sensitivity to climatic conditions: Scientific Reports, v. 8, no. 1, 11323, https://doi.org/10 .1038/s41598-018-29718-7.
- Cook, C.P., Van De Flierdt, T., Williams, T., Hemming, S.R., Iwai, M., Kobayashi, M., Jimenez-Espejo, F.J., Escutia, C., González, J.J., Khim, B.K., and McKay, R.M., 2013, Dynamic behaviour of the East Antarctic Ice Sheet during Pliocene warmth: Nature Geoscience, v. 6, no. 9, p. 765–769, https:// doi.org/10.1038/ngeo1889.
- Cook, C.P., Hemming, S.R., van de Flierdt, T., Davis, E.L.P., Williams, T., Galindo, A.L., Jimenez-Espejo, F.J., and Escutia, C., 2017, Glacial erosion of East Antarctica in the Pliocene: A comparative study of multiple marine sediment provenance tracers: Chemical Geology, v. 466, p. 199–218, https://doi.org/10.1016/j.chemgeo.2017.06.011.
- Cooper, J.A., Mortimer, G.E., Rosier, C.M., and Uppill, R.K., 1985, Gawler Range magmatism—Further isotopic age data: Australian Journal of Earth Sciences, v. 32, no. 2, p. 115–123, https://doi.org/10.1080/08120098508729318.
- Cox, S.E., Thomson, S.N., Reiners, P.W., Hemming, S.R., and Van De Flierdt, T., 2010, Extremely low long-term erosion rates around the Gamburtsev Mountains in interior East Antarctica: Geophysical Research Letters, v. 37, no. 22, L22307, https://doi.org/10.1029/2010GL045106.
- Danišík, M., McInnes, B.I., Kirkland, C.L., McDonald, B.J., Evans, N.J., and Becker, T., 2017, Seeing is believing: Visualization of He distribution in zircon and implications for thermal history reconstruction on single crystals: Science Advances, v. 3, no. 2, https://doi.org/10.1126/sciadv.1601121.
- De Santis, L., Prato, S., Brancolini, G., Lovo, M., and Torelli, L., 1999, The eastern Ross Sea continental shelf during the Cenozoic: Implications for the West Antarctic Ice Sheet development: Global and Planetary Change, v. 23, no. 1–4, p. 173–196, https://doi.org/10.1016/S0921-8181
- Diester-Haass, L., Robert, C., and Chamley, H., 1993, Paleoceanographic and paleoclimatic evolution in the Weddell Sea (Antarctica) during the middle Eocene–late Oligocene, from a coarse sediment fraction and clay mineral data (ODP Site 689): Marine Geology, v. 114, no. 3–4, p. 233–250, https:// doi.org/10.1016/0025-3227(93)90030-Y.
- Di Vincenzo, G., Talarico, F., and Kleinschmidt, G., 2007, An ⁴⁰Ar-³⁸Ar investigation of the Mertz glacier area (George V Land, Antarctica): Implications for the Ross orogen–East Antarctic craton relationship and Gondwana reconstructions: Precambrian Research, v. 152, no. 3–4, p. 93–118, https://doi.org/10.1016/j.precamres.2006.10.002.
- Duclaux, G., Rey, P., Guillot, S., and Ménot, R.P., 2007, Orogenparallel flow during continental convergence: Numerical experiments and Archean field examples: Geology, v. 35, no. 8, p. 715–718, https://doi.org/10.1130/G23540A.1.
- Duclaux, G., Rolland, Y., Ruffet, G., Ménot, R.P., Guillot, S., Peucat, J.J., Fanning, M., Rey, P., and Pêcher, A., 2008, Superimposed Neoarchaean and Paleoproterozoic tectonics in the Terre Adélie craton (East Antarctica): Evidence from Th-U-Pb ages on monazite and ⁴⁰Ar/⁵⁸Ar ages: Precambrian Research, v. 167, no. 3–4, p. 316–338, https://doi.org/10.1016/j.precamres.2008.09.009.

- Ehrmann, W.U., and Mackensen, A., 1992, Sedimentological evidence for the formation of an East Antarctic lee Sheet in Eocene/Oligocene time: Palaeogeography, Palaeoclimatology, Palaeoecology, v. 93, no. 1–2, p. 85–112, https://doi.org/10.1016/0031-0182/92)90185-8.
- Elliot, D.H., 1992, Jurassic magmatism and tectonism associated with Gondwanaland break-up: An Antarctic perspective, *in* Storey, B.C., Alabaster, T., and Pankhurst, R.J., eds., Magmatism and the Causes of Continental Break-Up: Geological Society, London, Special Publication 68, p. 165–184, https://doi.org/10.1144/GSL.SP.1992.068.01.11.
- Elliot, D.H., and Fleming, T.H., 2004, Occurrence and dispersal of magmas in the Jurassic Ferrar large igneous province, Antarctica: Gondwana Research, v. 7, no. 1, p. 223–237, https:// doi.org/10.1016/S1342-937X(05)70322-1.
- Elliot, D.H., and Fleming, T.H., 2018, The Ferrar large igneous province: Field and geochemical constraints on supracrustal (high-level) emplacement of the magmatic system, in Sensarma, S., and Storey, B.C., eds., Large Igenous Provinces from Gondwana and Adjacent Regions: Geological Society, London, Special Publication 463, p. 41–58, https://doi.org/10.1144/SP463.1.
- Escutia, C., De Santis, L., Donda, F., Dunbar, R.B., Cooper, A.K., Brancolini, G., and Eittreim, S.L., 2005, Cenozoic ice sheet history from East Antarctic Wilkes Land continental margin sediments: Global and Planetary Change, v. 45, no. 1–3, p. 51–81. https://doi.org/10.1016/j.gloplacha.2004.09.010.
- Escutia, C., Brinkhuis, H., and Klaus, A., 2011, IODP Expedition 318: From greenhouse to icehouse at the Wilkes Land Antarctic margin: Scientific Drilling, v. 12, p. 15–23, https://doi .org/10.2204/jodp.sd.12.02.2011.
- Estrada, S., Läufer, A., Eckelmann, K., Hofmann, M., Gärtner, A., and Linnemann, U., 2016, Continuous Neoproterozoic to Ordovician sedimentation at the East Gondwana margin—Implications from detrital zircons of the Ross orogen in northern Victoria Land, Antarctica: Gondwana Research, v. 37, p. 426–448, https://doi.org/10.1016/j.gr.2015.10.006.
- Federico, L., Capponi, G., and Crispini, L., 2006, The Ross orogeny of the Transantarctic Mountains: A northern Victoria Land perspective: International Journal of Earth Sciences, v. 95, no. 5, p. 759–770, https://doi.org/10.1007/s00531-005 -0063-5
- Ferraccioli, F., Armadillo, E., Jordan, T., Bozzo, E., and Corr, H., 2009, Aeromagnetic exploration over the East Antarctic Ice Sheet: A new view of the Wilkes Subglacial Basin: Tectonophysics, v. 478, no. 1–2, p. 62–77, https://doi.org/10.1016/j .tecto.2009.03.013.
- Fitzgerald, P.G., and Goodge, J.W., 2022, Exhumation and tectonic history of inaccessible subglacial interior East Antarctica from thermochronology on glacial erratics: Nature Communications, v. 13, no. 1, 6217, https://doi.org/10.1038/s41467-022-33791-y.
- Fleming, T.H., Heimann, A., Foland, K.A., and Elliot, D.H., 1997,

 40Ar/s9Ar geochronology of Ferrar Dolerite sills from the
 Transantarctic Mountains, Antarctica: Implications for the
 age and origin of the Ferrar magmatic province: Geological
 Society of America Bulletin, v. 109, no. 5, p. 533–546, https://doi.org/10.1130/0016-7606(1997)109<0533:AAGOFD>2.3
- Flowers, R.M., Ketcham, R.A., Shuster, D.L., and Farley, K.A., 2009, Apatite (U-Th)/He thermochronometry using a

- radiation damage accumulation and annealing model: Geochimica et Cosmochimica Acta, v. 73, no. 8, p. 2347–2365, https://doi.org/10.1016/j.gca.2009.01.015.
- Foster, D.A., and Ehlers, K., 1998, 40Ar-39Ar thermochronology of the southern Gawler craton, Australia: Implications for Mesoproterozoic and Neoproterozoic tectonics of East Gondwana and Rodinia: Journal of Geophysical Research: Solid Earth, v. 103, no. B5, p. 10,177–10,193, https://doi.org/10.1029/98J800151.
- Fox, M., Tripathy-Lang, A., Shuster, D.L., Winn, C., Karlstrom, K., and Kelley, S., 2017, Westernmost Grand Canyon incision: Testing thermochronometric resolution: Earth and Planetary Science Letters, v. 474, p. 248–256, https://doi.org/10.1016 /j.epsl.201706.049.
- Fretwell, P., Pritchard, H.D., Vaughan, D.G., Bamber, J.L., Barrand, N.E., Bell, R., Bianchi, C., Bingham, R.G., Blankenship, D.D., Casassa, G., and Catania, G., 2013, Bedmap2: Improved ice bed, surface and thickness datasets for Antarctica: The Cryosphere, v. 7, no. 1, p. 375–393, https://doi.org/10.5194 /tc-7-375-2013.
- Gasson, E., DeConto, R., and Pollard, D., 2015, Antarctic bedrock topography uncertainty and ice sheet stability: Geophysical Research Letters, v. 42, no. 13, p. 5372–5377, https://doi.org /10.1002/2015GL064322.
- Gasson, E., DeConto, R.M., Pollard, D., and Levy, R.H., 2016, Dynamic Antarctic ice sheet during the early to mid-Miocene: Proceedings of the National Academy of Sciences of the United States of America, v. 113, no. 13, p. 3459–3464, https://doi.org/10.1073/pnas.1516130113.
- Gehrels, G., Valencia, V., and Pullen, A., 2006, Detrital zircon geochronology by laser-ablation multicollector ICPMS at the Arizona LaserChron Center: The Paleontological Society Papers, v. 12, p. 67–76, https://doi.org/10.1017 /51089332600001352.
- Gehrels, G.E., Valencia, V.A., and Ruiz, J., 2008, Enhanced precision, accuracy, efficiency, and spatial resolution of U-Pb ages by laser ablation–multicollector–inductively coupled plasma–mass spectrometry: Geochemistry, Geophysics, Geosystems, v. 9, no. 3, https://doi.org/10.1029/2007GC001805.
- Goodge, J.W., 2007, Metamorphism in the Ross orogen and its bearing on Gondwana margin tectonics, in Cloos, M., Carlson, W.D., Gilbert, M.C., Liou, J.G., and Sorensen, S.S., eds., Convergent Margin Tectonics and Associated Regions: A Tribute to W.G. Ernst: Geological Society of America Special Paper 419, p. 185–203, https://doi.org/10.1130/2006 .2419(10).
- Goodge, J.W., Myrow, P., Williams, I.S., and Bowring, S.A., 2002, Age and provenance of the Beardmore Group, Antarctica: Constraints on Rodinia supercontinent breakup: The Journal of Geology, v. 110, no. 4, p. 393–406, https://doi.org/10 .1086/340629.
- Goodge, J.W., Vervoort, J.D., Fanning, C.M., Brecke, D.M., Farmer, G.L., Williams, I.S., Myrow, P.M., and DePaolo, D.J., 2008, A positive test of East Antarctica–Laurentia juxtaposition within the Rodinia supercontinent: Science, v. 321, no. 5886, p. 235–240, https://doi.org/10.1126/science.1159189.
- Goodge, J.W., Fanning, C.M., Brecke, D.M., Licht, K.J., and Palmer, E.F., 2010, Continuation of the Laurentian Grenville Province across the Ross Sea margin of East Antarctica: The Journal of Geology, v. 118, no. 6, p. 601–619, https:// doi.org/10.1086/656385.

- Goodge, J.W., Fanning, C.M., Fisher, C.M., and Vervoort, J.D., 2017, Proterozoic crustal evolution of central East Antarctica: Age and isotopic evidence from glacial igneous clasts, and links with Australia and Laurentia: Precambrian Research, v. 299, p. 151–176, https://doi.org/10.1016/j.precamres.2017.07026.
- Grove, M., and Harrison, T.M., 1996, ⁴⁰Ar* diffusion in Fe-rich biotite: The American Mineralogist, v. 81, no. 7–8, p. 940–951, https://doi.org/10.2138/am-1996-7-816.
- Guenthner, W.R., Reiners, P.W., Ketcham, R.A., Nasdala, L., and Giester, G., 2013, Helium diffusion in natural zircon: Radiation damage, anisotropy, and the interpretation of zircon (U-Th)/He thermochronology: American Journal of Science, v. 313, no. 3, p. 145–198, https://doi.org/10.2475/03.2013.01.
- Halberstadt, A.R.W., Chorley, H., Levy, R.H., Naish, T., DeConto, R.M., Gasson, E., and Kowalewski, D.E., 2021, CO₂ and tectonic controls on Antarctic climate and ice-sheet evolution in the mid-Miocene: Earth and Planetary Science Letters, v. 564, https://doi.org/10.1016/j.epsl.2021.116908.
- Hauptvogel, D.W., and Passchier, S., 2012, Early-middle Miocene (17–14 Ma) Antarctic ice dynamics reconstructed from the heavy mineral provenance in the AND-2A drill core, Ross Sea, Antarctica: Global and Planetary Change, v. 82, p. 38–50, https://doi.org/10.1016/j.gloplacha.2011.11.003.
- Hauptvogel, D.W., Pekar, S.F., and Pincay, V., 2017, Evidence for a heavily glaciated Antarctica during the late Oligocene "warming" (27.8–24.5 Ma): Stable isotope records from ODP Site 690: Paleoceanography, v. 32, no. 4, p. 384–396, https:// doi.org/10.1002/2016PA002972.
- Hochmuth, K., Gohl, K., Leitchenkov, G., Sauermilch, I., Whittaker, J.M., Uenzelmann-Neben, G., Davy, B., and De Santis, L., 2020, The evolving paleobathymetry of the circum-Antarctic Southern Ocean since 34 Ma: A key to understanding past cryosphere-ocean developments: Geochemistry, Geophysics, Geosystems, v. 21, no. 8, https://doi.org/10.1029/2020GC009122.
- lizuka, M., Seki, O., Wilson, D.J., Suganuma, Y., Horikawa, K., van de Flierdt, T., Ikehara, M., et al., 2023, Multiple episodes of ice loss from the Wilkes Subglacial Basin during the Last Interglacial: Nature Communications, v. 14, no. 1, 2129, https://doi.org/10.1038/s41467-023-37325-y.
- Integrated Ocean Drilling Program (IODP) Expedition 318 Scientists, 2011a, Site U1358, in Escutia, C., Brinkhuis, H., Klaus, A., and the Expedition 318 Scientists, Proceedings of the Integrated Ocean Drilling Program Volume 318: Tokyo, Integrated Ocean Drilling Program Management International, Inc., p. 1–16, https://doi.org/10.2204/iodp.proc.318.106.2011.
- Integrated Ocean Drilling Program (IODP) Expedition 318 Scientists, 2011b, Site U1360, in Escutia, C., Brinkhuis, H., Klaus, A., and the Expedition 318 Scientists, Proceedings of the Integrated Ocean Drilling Program Volume 318: Tokyo, Integrated Ocean Drilling Program Management International, Inc., p. 1–23, https://doi.org/10.2204/jodp.proc.318.108.2011.
- Jamieson, S.S., Hulton, N.R., and Hagdorn, M., 2008, Modelling landscape evolution under ice sheets: Geomorphology, v. 97, no. 1–2, p. 91–108, https://doi.org/10.1016/j.geomorph .2007.02.047.
- Jamieson, S.S., Sugden, D.E., and Hulton, N.R., 2010, The evolution of the subglacial landscape of Antarctica: Earth and Planetary Science Letters, v. 293, no. 1–2, p. 1–27, https:// doi.org/10.1016/j.epsl.2010.02.012.

- Jamieson, S.S., Ross, N., Paxman, G.J., Clubb, F.J., Young, D.A., Yan, S., Greenbaum, J., Blankenship, D.D., and Siegert, M.J., 2023, An ancient river landscape preserved beneath the East Antarctic Ice Sheet: Nature Communications, v. 14, no. 1, 6507, https://doi.org/10.1038/s41467-023-42152-2.
- Johnson, J.E., Flowers, R.M., Baird, G.B., and Mahan, K.H., 2017, "Inverted" zircon and apatite (U-Th)/He dates from the Front Range, Colorado: High-damage zircon as a low-temperature (<50 °C) thermochronometer: Earth and Planetary Science Letters, v. 466, p. 80–90, https://doi.org/10.1016/j.epsl.2017 03 002
- Jordan, T.A., Ferraccioli, F., Armadillo, E., and Bozzo, E., 2013, Crustal architecture of the Wilkes Subglacial Basin in East Antarctica, as revealed from airborne gravity data: Tectonophysics, v. 585, p. 196–206, https://doi.org/10.1016/j.tecto .2012.06.041.
- Kessler, M.A., Anderson, R.S., and Briner, J.P., 2008, Fjord insertion into continental margins driven by topographic steering of ice: Nature Geoscience, v. 1, no. 6, p. 365–369, https://doi.org/10.1038/ngeo201.
- Ketcham, R.A., 2005, Forward and inverse modeling of low-temperature thermochronometry data: Reviews in Mineralogy and Geochemistry, v. 58, no. 1, p. 275–314, https:// doi.org/10.2138/rmq.2005.58.11.
- Ketcham, R.A., Donelick, R.A., and Carlson, W.D., 1999, Variability of apatite fission-track annealing kinetics: Ill. Extrapolation to geological time scales: The American Mineralogist, v. 84, no. 9, p. 1235–1255, https://doi.org/10.2138/am-1999-0903.
- Ketcham, R.A., Carter, A., Donelick, R.A., Barbarand, J., and Hurford, A.J., 2007, Improved modeling of fission-track annealing in apatite: The American Mineralogist, v. 92, no. 5–6, p. 799–810, https://doi.org/10.2138/am.2007.2281.
- Kulhanek, D.K., Levy, R.H., Clowes, C.D., Prebble, J.G., Rodelli, D., Jovane, L., Morgans, H.E., Kraus, C., Zwingmann, H., Griffith, E.M., and Scher, H.D., 2019, Revised chronostratigraphy of DSDP Site 270 and late Oligocene to early Miocene paleoecology of the Ross Sea sector of Antarctica: Global and Planetary Change, v. 178, p. 46–64, https://doi.org/10.1016/j .gloplacha.2019.04.002.
- Lamarque, G., Bascou, J., Ménot, R.P., Paquette, J.L., Couzinié, S., Rolland, Y., and Cottin, J.Y., 2018, Ediacaran to Lower Cambrian basement in eastern George V Land (Antarctica): Evidence from U-Pb dating of gneiss xenoliths and implications for the South Australia–East Antarctica connection: Lithos, v. 318, p. 219–229, https://doi.org/10.1016 /i.lithos.2018.08.021.
- Levy, R., Harwood, D., Florindo, F., Sangiorgi, F., Tripati, R., Von Eynatten, H., Gasson, E., Kuhn, G., Tripati, A., DeConto, R., and Fielding, C., 2016, Antarctic ice sheet sensitivity to atmospheric CO₂ variations in the early to mid-Miocene: Proceedings of the National Academy of Sciences of the United States of America, v. 113, no. 13, p. 3453–3458, https://doi .org/10.1073/pnas.1516030113.
- Lewis, A.R., Marchant, D.R., Ashworth, A.C., Hemming, S.R., and Machlus, M.L., 2007, Major middle Miocene global climate change: Evidence from East Antarctica and the Transantarctic Mountains: Geological Society of America Bulletin, v. 119, no. 11–12, p. 1449–1461, https://doi.org/10.1130/0016 -7606(2007)119[1449:MMMGCC]2.0.CO;2.
- Lewis, A.R., Marchant, D.R., Ashworth, A.C., Hedenäs, L., Hemming, S.R., Johnson, J.V., Leng, M.J., Machlus, M.L., Newton,

- A.E., Raine, J.I., and Willenbring, J.K., 2008, Mid-Miocene cooling and the extinction of tundra in continental Antarctica: Proceedings of the National Academy of Sciences of the United States of America, v. 105, no. 31, p. 10,676–10,680, https://doi.org/10.1073/pnas.0802501105.
- Licht, K.J., and Hemming, S.R., 2017, Analysis of Antarctic glacigenic sediment provenance through geochemical and petrologic applications: Quaternary Science Reviews, v. 164, p. 1–24, https://doi.org/10.1016/j.quascirev.2017.03.009.
- Licht, K.J., Hennessy, A.J., and Welke, B.M., 2014, The U-Pb detrital zircon signature of West Antarctic ice stream tills in the Ross embayment, with implications for Last Glacial Maximum ice flow reconstructions: Antarctic Science, v. 26, no. 6, p. 687–697, https://doi.org/10.1017/S0954102014000315.
- Liebrand, D., de Bakker, A.T., Beddow, H.M., Wilson, P.A., Bohaty, S.M., Ruessink, G., Pälike, H., Batenburg, S.J., Hilgen, F.J., Hodell, D.A., and Huck, C.E., 2017, Evolution of the early Antarctic ice ages: Proceedings of the National Academy of Sciences of the United States of America, v. 114, no. 15, p. 3867–3872, https://doi.org/10.1073/pnas.1615440114.
- Lindeque, A., Gohl, K., Wobbe, F., and Uenzelmann-Neben, G., 2016, Preglacial to glacial sediment thickness grids for the southern Pacific margin of West Antarctica: Geochemistry, Geophysics, Geosystems, v. 17, no. 10, p. 4276–4285, https:// doi.org/10.1002/2016GC006401.
- Lisker, F., 2002, Review of fission track studies in northern Victoria Land, Antarctica—Passive margin evolution versus uplift of the Transantarctic Mountains: Tectonophysics, v. 349, no. 1–4, p. 57–73, https://doi.org/10.1016/S0040-1951 (02)00046-X.
- Lisker, F., and Olesch, M., 2003, Long-term landscape evolution of George V Land as indicated by fission track data: Terra Antartica, v. 10, p. 249–256.
- Lisker, F., Brown, R., and Fabel, D., 2003, Denudational and thermal history along a transect across the Lambert graben, northern Prince Charles Mountains, Antarctica, derived from apatite fission track thermochronology: Tectonics, v. 22, no. 5, p. 1055, https://doi.org/10.1029/2002TC001477.
- Maritati, A., Halpin, J.A., Whittaker, J.M., and Daczko, N.R., 2019, Fingerprinting Proterozoic bedrock in interior Wilkes Land, East Antarctica: Scientific Reports, v. 9, no. 1, 10192, https:// doi.org/10.1038/s41598-019-46612-y.
- Maritati, A., Danišík, M., Halpin, J.A., Whittaker, J.M., and Aitken, A.R., 2020, Pangea rifting shaped the East Antarctic landscape: Tectonics, v. 39, no. 8, https://doi.org/10.1029 /2020TC006180.
- McKay, R., Naish, T., Carter, L., Riesselman, C., Dunbar, R., Sjunneskog, C., Winter, D., Sangiorgi, F., Warren, C., Pagani, M., and Schouten, S., 2012, Antarctic and Southern Ocean influences on late Pliocene global cooling: Proceedings of the National Academy of Sciences of the United States of America, v. 109, no. 17, p. 6423–6428, https://doi.org/10.1073/pnas.1112248109.
- Mengel, M., and Levermann, A., 2014, Ice plug prevents irreversible discharge from East Antarctica: Nature Climate Change, v. 4, no. 6, p. 451–455, https://doi.org/10.1038/nclimate2226.
- Ménot, R.P., Duclaux, G., Peucat, J.J., Rolland, Y., Guillot, S., Fanning, M., Bascou, J., Gapais, D., and Pêcher, A., 2007, Geology of the Terre Adélie craton (135–146°E), in Cooper, A.K., and Raymond, C.R., et al., eds., Antarctica: A Keystone in a Changing World (Online Proceedings of the 10th ISAES):

- U.S. Geological Survey Open-File Report 1047, https://doi.org/10.3133/of2007-1047.srp048.
- Mezger, K., and Krogstad, E.J., 1997, Interpretation of discordant U-Pb zircon ages: An evaluation: Journal of Metamorphic Geology, v. 15, no. 1, p. 127–140, https://doi.org/10.1111/j.1525-1314.199700008.x.
- Morlighem, M., Rignot, E., Binder, T., Blankenship, D., Drews, R., Eagles, G., Eisen, O., Ferraccioli, F., Forsberg, R., Fretwell, P., and Goel, V., 2020, Deep glacial troughs and stabilizing ridges unveiled beneath the margins of the Antarctic ice sheet: Nature Geoscience, v. 13, no. 2, p. 132–137, https:// doi.org/10.1038/s41561-019-0510-8.
- Murray, K.E., Reiners, P.W., and Thomson, S.N., 2016, Rapid Pliocene–Pleistocene erosion of the central Colorado Plateau documented by apatite thermochronology from the Henry Mountains: Geology, v. 44, no. 6, p. 483–486, https:// doi.org/10.1130/G37733.1.
- Naish, T.R., Woolfe, K.J., Barrett, P.J., Wilson, G.S., Atkins, C., Bohaty, S.M., Bücker, C.J., Claps, M., Davey, F.J., Dunbar, G.B., and Dunn, A.G., 2001, Orbitally induced oscillations in the East Antarctic ice sheet at the Oligocene/Miocene boundary: Nature, v. 413, no. 6857, p. 719–723, https://doi.org/10.1038/35099534.
- Nasdala, L., Hanchar, J.M., Kronz, A., and Whitehouse, M.J., 2005, Long-term stability of alpha particle damage in natural zircon: Chemical Geology, v. 220, no. 1–2, p. 83–103, https:// doi.org/10.1016/j.chemgeo.2005.03.012.
- Naumenko-Dèzes, M.O., Rolland, Y., Lamarque, G., Duclaux, G., Gallet, S., Bascou, J., and Ménot, R.P., 2020, Petrochronology of the Terre Adélie craton (East Antarctica) evidences a long-lasting Proterozoic (1.7–1.5 Ga) tectono-metamorphic evolution—Insights for the connections with the Gawler craton and Laurentia: Gondwana Research, v. 81, p. 21–57, https://doi.org/10.1016/j.gr.2019.11.010.
- Naylor, S., Wickert, A.D., Edmonds, D.A., and Yanites, B.J., 2021, Landscape evolution under the southern Laurentide ice sheet: Science Advances, v. 7, no. 48, p. 1–9, https://doi.org/10.1126/sciadv.abi2938.
- Paxman, G.J., Jamieson, S.S., Ferraccioli, F., Bentley, M.J., Ross, N., Armadillo, E., Gasson, E.G., Leitchenkov, G., and DeConto, R.M., 2018, Bedrock erosion surfaces record former East Antarctic Ice Sheet extent: Geophysical Research Letters, v. 45, no. 9, p. 4114–4123, https://doi.org/10.1029 /2018GL077268.
- Paxman, G.J., Jamieson, S.S., Hochmuth, K., Gohl, K., Bentley, M.J., Leitchenkov, G., and Ferraccioli, F., 2019a, Reconstructions of Antarctic topography since the Eocene-Oligocene boundary: Palaeogeography, Palaeoclimatology, Palaeoecology, v. 535, https://doi.org/10.1016/j.palaeo.2019.109346.
- Paxman, G.J., Jamieson, S.S., Ferraccioli, F., Bentley, M.J., Ross, N., Watts, A.B., Leitchenkov, G., Armadillo, E., and Young, D.A., 2019b, The role of lithospheric flexure in the landscape evolution of the Wilkes Subglacial Basin and Transantarctic Mountains, East Antarctica: Journal of Geophysical Research: Earth Surface, v. 124, no. 3, p. 812–829, https://doi.org/10.1029/2018JF004705.
- Paxman, G.J., Gasson, E.G., Jamieson, S.S., Bentley, M.J. and Ferraccioli, F., 2020, Long-term increase in Antarctic Ice Sheet vulnerability driven by bed topography evolution: Geophysical Research Letters, v. 47, no. 20, https://doi.org/10.1029/2020GL090003.

- Payne, J.L., Hand, M., Barovich, K.M., Reid, A., and Evans, D.A., 2009, Correlations and reconstruction models for the 2500– 1500 Ma evolution of the Mawson continent, in Reddy, S.M., et al., eds., Palaeoproterozoic Supercontinents and Global Evolution: Geological Society, London, Special Publication 323, p. 319–355, https://doi.org/10.1144/SP323.16.
- Peucat, J.J., Ménot, R.P., Monnier, O., and Fanning, C.M., 1999, The Terre Adélie basement in the East-Antarctica Shield: Geological and isotopic evidence for a major 1.7 Ga thermal event; comparison with the Gawler craton in South Australia: Precambrian Research, v. 94, no. 3–4, p. 205–224, https://doi.org/10.1016/S0301-9268(98)00119-3.
- Peucat, J.J., Capdevila, R., Fanning, C.M., Ménot, R.P., Pécora, L., and Testut, L., 2002, 1.60 Ga felsic volcanic blocks in the moraines of the Terre Adélie craton, Antarctica: Comparisons with the Gawler Range volcanics, South Australia: Australian Journal of Earth Sciences, v. 49, no. 5, p. 831–845, https://doi.org/10.1046/j.1440-0952.2002.00956.x.
- Pierce, E.L., Williams, T., Van De Flierdt, T., Hemming, S.R., Goldstein, S.L., and Brachfeld, S.A., 2011, Characterizing the sediment provenance of East Antarctica's weak underbelly: The Aurora and Wilkes sub-glacial basins: Paleoceanography, v. 26, no. 4, https://doi.org/10.1029/2011PA002127.
- Pierce, E.L., Hemming, S.R., Williams, T., van de Flierdt, T., Thomson, S.N., Reiners, P.W., Gehrels, G.E., Brachfeld, S.A., and Goldstein, S.L., 2014, A comparison of detrital U-Pb zircon, ⁴⁰Ar/⁸⁹Ar hornblende, ⁴⁰Ar/⁸⁹Ar biotite ages in marine sediments off East Antarctica: Implications for the geology of subglacial terrains and provenance studies: Earth-Science Reviews, v. 138, p. 156–178, https://doi.org/10.1016/j.earscirev.2014.08.010.
- Pierce, E.L., van de Flierdt, T., Williams, T., Hemming, S.R., Cook, C.P., and Passchier, S., 2017, Evidence for a dynamic East Antarctic Ice Sheet during the mid-Miocene climate transition: Earth and Planetary Science Letters, v. 478, p. 1–13, https://doi.org/10.1016/j.epsl.2017.08.011.
- Pollard, D., and DeConto, R.M., 2020, Continuous simulations over the last 40 million years with a coupled Antarctic ice sheet-sediment model: Palaeogeography, Palaeoclimatology, Palaeoecology, v. 537, https://doi.org/10.1016/j.palaeo .2019.109374.
- Reiners, P.W., and Brandon, M.T., 2006, Using thermochronology to understand orogenic erosion: Annual Review of Earth and Planetary Sciences, v. 34, p. 419–466, https://doi.org/10.1146/ /annurev.earth.34.031405.125202.
- Reiners, P.W., Farley, K.A., and Hickes, H.J., 2002, He diffusion and (U-Th)/He thermochronometry of zircon: Initial results from Fish Canyon Tuff and Gold Butte: Tectonophysics, v. 349, no. 1–4, p. 297–308, https://doi.org/10.1016/S0040 -1951(02)00058-6.
- Reiners, P.W., Thomson, S.N., McPhillips, D., Donelick, R.A., and Roering, J.J., 2007, Wildfire thermochronology and the fate and transport of apatite in hillslope and fluvial environments: Journal of Geophysical Research: Earth Surface, v. 112, no. F4, F04001, https://doi.org/10.1029/2007JF000759.
- Reiners, P.W., Carlson, R.W., Renne, P.R., Cooper, K.M., Granger, D.E., McLean, N.M., and Schoene, B., 2017, Geochronology and Thermochronology: Chichester, UK, John Wiley & Sons, 480 p., https://doi.org/10.1002/9781118455876.
- Rignot, E., Mouginot, J., and Scheuchl, B., 2011, Ice flow of the Antarctic ice sheet: Science, v. 333, no. 6048, p. 1427–1430, https://doi.org/10.1126/science.1208336.

- Robert, C., and Kennett, J.P., 1997, Antarctic continental weathering changes during Eocene-Oligocene cryosphere expansion: Clay mineral and oxygen isotope evidence: Geology, v. 25, no. 7, p. 587–590, https://doi.org/10.1130/0091-7613(1997)025-0587-ACWCDE>-2.3.CO:2.
- Roberts, A.P., Wilson, G.S., Harwood, D.M., and Verosub, K.L., 2003, Glaciation across the Oligocene-Miocene boundary in southern McMurdo Sound, Antarctica: New chronology from the CIROS-1 drill hole: Palaeogeography, Palaeoclimatology, Palaeoecology, v. 198, no. 1–2, p. 113–130, https://doi.org/10.1016/S0031-0182(03)00399-7.
- Rolland, Y., Bernet, M., van der Beek, P., Gautheron, C., Duclaux, G., Bascou, J., Balvay, M., Héraudet, L., Sue, C., and Ménot, R.P., 2019, Late Paleozoic ice age glaciers shaped East Antarctica landscape: Earth and Planetary Science Letters, v. 506, p. 123–133, https://doi.org/10.1016 /j.epsl.2018.10.044.
- Röthlisberger, H., and Iken, A., 1981, Plucking as an effect of waterpressure variations at the glacier bed: Annals of Glaciology, v. 2, p. 57–62, https://doi.org/10.3189/172756481794352144.
- Roy, M., van de Flierdt, T., Hemming, S.R., and Goldstein, S.L., 2007, 40Ar/39Ar ages of hornblende grains and bulk Sm/Nd isotopes of circum-Antarctic glacio-marine sediments: Implications for sediment provenance in the Southern Ocean: Chemical Geology, v. 244, no. 3–4, p. 507–519, https:// doi.org/10.1016/j.chemgeo.2007.07.017.
- Sagnotti, L., Florindo, F., Verosub, K.L., Wilson, G.S., and Roberts, A.P., 1998, Environmental magnetic record of Antarctic palaeoclimate from Eocene/Oligocene glaciomarine sediments, Victoria Land Basin: Geophysical Journal International, v. 134, no. 3, p. 653–662, https://doi.org/10.1046/j .1365-246x.1998.00559.x.
- Sauermilch, I., Whittaker, J.M., Bijl, P.K., Totterdell, J.M., and Jokat, W., 2019, Tectonic, oceanographic, and climatic controls on the Cretaceous–Cenozoic sedimentary record of the Australian-Antarctic Basin: Journal of Geophysical Research: Solid Earth, v. 124, no. 8, p. 7699–7724, https:// doi.org/10.1029/2018JB016683.
- Schaltegger, U., Fanning, C.M., Günther, D., Maurin, J.C., Schulmann, K., and Gebauer, D., 1999, Growth, annealing and recrystallization of zircon and preservation of monazite in high-grade metamorphism: Conventional and in-situ U-Pb isotope, cathodoluminescence and microchemical evidence: Contributions to Mineralogy and Petrology, v. 134, no. 2, p. 186–201, https://doi.org/10.1007/s004100050478.
- Schoof, C., 2007, Ice sheet grounding line dynamics: Steady states, stability, and hysteresis: Journal of Geophysical Research: Earth Surface, v. 112, no. F3, F03S28, https://doi .org/10.1029/2006JF000664.
- Shevenell, A.E., Kennett, J.P., and Lea, D.W., 2004, Middle Miocene Southern Ocean cooling and Antarctic cryosphere expansion: Science, v. 305, no. 5691, p. 1766–1770, https://doi.org/10.1126/science.1100061.
- Siegert, M.J., 2000, Antarctic subglacial lakes: Earth-Science Reviews, v. 50, no. 1–2, p. 29–50, https://doi.org/10.1016 /S0012-8252(99)00068-9.
- Siegert, M.J., Taylor, J., and Payne, A.J., 2005, Spectral roughness of subglacial topography and implications for former ice-sheet dynamics in East Antarctica: Global and Planetary Change, v. 45, no. 1–3, p. 249–263, https://doi.org/10.1016/j.gloplacha.2004.09.008.

- Sirevaag, H., Jacobs, J., and Ksienzyk, A.K., 2021, Substantial spatial variation in glacial erosion rates in the Dronning Maud Land Mountains, East Antarctica: Communications Earth & Environment, v. 2, 244, https://doi.org/10.1038 /s43247-021-00315-3.
- Stål, T., Reading, A.M., Halpin, J.A., Phipps, S.J., and Whittaker, J.M., 2020, The Antarctic crust and upper mantle: A flexible 3D model and software framework for interdisciplinary research: Frontiers of Earth Science, v. 8, https://doi.org/10 .3389/feart.2020.577502
- Straume, E.O., Gaina, C., Medvedev, S., Hochmuth, K., Gohl, K., Whittaker, J.M., Abdul Fattah, R., Doornenbal, J.C., and Hopper, J.R., 2019, GlobSed: Updated total sediment thickness in the world's oceans: Geochemistry, Geophysics, Geosystems, v. 20, no. 4, p. 1756–1772, https://doi.org/10.1029/2018GC008115.
- Swain, C.J., and Kirby, J.F., 2021, Effective elastic thickness map reveals subglacial structure of East Antarctica: Geophysical Research Letters, v. 48, https://doi.org/10.1029 /2020GL091576.
- Tauxe, L., Stickley, C.E., Sugisaki, S., Bijl, P.K., Bohaty, S.M., Brinkhuis, H., Escutia, C., Flores, J.A., Houben, A.J.P., Iwai, M., and Jiménez-Espejo, F., 2012, Chronostratigraphic framework for the IODP Expedition 318 cores from the Wilkes Land margin: Constraints for paleoceanographic reconstruction: Paleoceanography, v. 27, no. 2, https://doi.org/10.1029 /2012PA002308.
- Thomson, S.N., Gehrels, G.E., Ruiz, J., and Buchwaldt, R., 2012, Routine low-damage apatite U-Pb dating using laser ablation-multicollector-ICPMS: Geochemistry, Geophysics, Geosystems, v. 13, no. 2, Q0AA21, https://doi.org/10.1029 /2011GC003928.
- Thomson, S.N., Reiners, P.W., Hemming, S.R., and Gehrels, G.E., 2013, The contribution of glacial erosion to shaping the hidden landscape of East Antarctica: Nature Geoscience, v. 6, no. 3, p. 203–207, https://doi.org/10.1038/ngeo1722.
- Tochilin, C.J., Reiners, P.W., Thomson, S.N., Gehrels, G.E., Hemming, S.R., and Pierce, E.L., 2012, Erosional history of the

- Prydz Bay sector of East Antarctica from detrital apatite and zircon geo- and thermochronology multidating: Geochemistry, Geophysics, Geosystems, v. 13, no. 11, Q11015, https://doi.org/10.1029/2012GC004364.
- Veevers, J.J., 2012, Reconstructions before rifting and drifting reveal the geological connections between Antarctica and its conjugates in Gondwanaland: Earth-Science Reviews, v. 111, no. 3–4, p. 249–318, https://doi.org/10.1016/j.earscirev .2011.11.009.
- Voisine, E., Rolland, Y., Bernet, M., Carcaillet, J., Duclaux, G., Bascou, J., Sue, C., Balvay, M., and Ménot, R.P., 2020, Antarctic erosion history reconstructed by Terre Adélie moraine geochronology: Antarctic Science, v. 32, no. 5, p. 382–395, https://doi.org/10.1017/S095410202000036X.
- Welke, B., Licht, K., Hennessy, A., Hemming, S., Pierce Davis, E., and Kassab, C., 2016, Applications of detrital geochronology and thermochronology from glacial deposits to the Paleozoic and Mesozoic thermal history of the Ross Embayment, Antarctica: Geochemistry, Geophysics, Geosystems, v. 17, no. 7, p. 2762–2780, https://doi.org/10.1002/2015GC005941.
- Willett, C.D., Fox, M., and Shuster, D.L., 2017, A helium-based model for the effects of radiation damage annealing on helium diffusion kinetics in apatite: Earth and Planetary Science Letters, v. 477, p. 195–204, https://doi.org/10.1016 /j.epsl.2017.07.047.
- Williams, I.S., and Ellis, D.J., 1997, Pb, U and Th diffusion in natural zircon: Nature, v. 390, no. 6656, p. 159–162, https:// doi.org/10.1038/36554.
- Williams, T., van de Flierdt, T., Hemming, S.R., Chung, E., Roy, M., and Goldstein, S.L., 2010, Evidence for iceberg armadas from East Antarctica in the Southern Ocean during the late Miocene and early Pliocene: Earth and Planetary Science Letters, v. 290, no. 3–4, p. 351–361, https://doi.org/10.1016 /j.epsl.2009.12.031.
- Wilson, D.J., Bertram, R.A., Needham, E.F., van de Flierdt, T., Welsh, K.J., McKay, R.M., Mazumder, A., Riesselman, C.R., Jimenez-Espejo, F.J., and Escutia, C., 2018, Ice loss from the East Antarctic Ice Sheet during late Pleistocene interglacials:

- Nature, v. 561, no. 7723, p. 383–386, https://doi.org/10.1038/s41586-018-0501-8.
- Wilson, D.S., Pollard, D., DeConto, R.M., Jamieson, S.S., and Luyendyk, B.P., 2013, Initiation of the West Antarctic Ice Sheet and estimates of total Antarctic ice volume in the earliest Oligocene: Geophysical Research Letters, v. 40, no. 16, p. 4305–4309, https://doi.org/10.1002/qrl.50797.
- Winn, C., Karlstrom, K.E., Shuster, D.L., Kelley, S., and Fox, M., 2017, 6 Ma age of carving westernmost Grand Canyon: Reconciling geologic data with combined AFT, (U-Th)/He, and ⁴He/³He thermochronologic data: Earth and Planetary Science Letters, v. 474, p. 257–271, https://doi.org/10.1016 /j.epsl.2017.06.051.
- Winnick, M.J., and Caves, J.K., 2015, Oxygen isotope massbalance constraints on Pliocene sea level and East Antarctic Ice Sheet stability: Geology, v. 43, no. 10, p. 879–882, https:// doi.org/10.1130/G36999.1.
- Yamada, R., Murakami, M., and Tagami, T., 2007, Statistical modelling of annealing kinetics of fission tracks in zircon: Reassessment of laboratory experiments: Chemical Geology, v. 236, no. 1–2, p. 75–91, https://doi.org/10.1016/j .chemgeo.2006.09.002.
- Young, D.A., Wright, A.P., Roberts, J.L., Warner, R.C., Young, N.W., Greenbaum, J.S., Schroeder, D.M., Holt, J.W., Sugden, D.E., Blankenship, D.D., and van Ommen, T.D., 2011, A dynamic early East Antarctic Ice Sheet suggested by ice-covered fjord landscapes: Nature, v. 474, no. 7349, p. 72–75, https://doi.org/10.1038/nature10114.
- Zachos, J., Pagani, M., Sloan, L., Thomas, E., and Billups, K., 2001, Trends, rhythms, and aberrations in global climate 65 Ma to present: Science, v. 292, no. 5517, p. 686–693, https://doi.org/10.1126/science.1059412.
- Zattin, M., Andreucci, B., Thomson, S.N., Reiners, P.W., and Talarico, F.M., 2012, New constraints on the provenance of the ANDRILL AND-2A succession (western Ross Sea, Antarctica) from apatite triple dating: Geochemistry, Geophysics, Geosystems, v. 13, no. 10, Q10016, https://doi.org/10.1029/2012GC004357.